European summer weather linked to North Atlantic freshwater events in preceding years

Marilena Oltmanns[1], N. Penny Holliday[1], James Screen[2], Ben I. Moat[1], Simon A. Josey[1], D. Gwyn Evans[1], and Sheldon Bacon[1]

[1]National Oceanography Centre, Southampton, UK
[2]University of Exeter, Exeter, UK

Correspondence: Marilena Oltmanns (marilena.oltmanns@noc.ac.uk)

Abstract. Amplified Arctic ice loss in recent decades has been linked to increased occurrence of extreme mid-latitude weather. The underlying mechanisms remain elusive, however. One potential link occurs through the ocean as the loss of sea ice and glacial ice leads to increased freshwater fluxes into the North Atlantic. Thus, in this study, we examine the extent to which North Atlantic freshwater anomalies constrain the subsequent ocean-atmosphere evolution and assess their implications for European summer weather. Combining remote sensing, atmospheric reanalyses and model simulations, we show that stronger freshwater anomalies are associated with sharper sea surface temperature gradients over the North Atlantic in winter, destabilising the overlying atmosphere and inducing a northward shift in the North Atlantic Current. In turn, the jet stream over the North Atlantic is deflected northward in the following summers, leading to warmer and drier weather over Europe. Our results suggest that growing freshwater fluxes into the North Atlantic will increase the risk of heat waves and droughts over the coming decades, and could yield enhanced predictability of European summer weather, months to years in advance.

1 Introduction

Arctic near-surface temperature is currently warming twice as fast as the global average (Cohen et al., 2019), which manifests itself in an average sea ice volume loss of $3.0 \pm 0.2 \cdot 1000$ km^3 decade^{-1}, based on the period 1979 to 2018 (Kumar et al., 2020). Similarly large losses are observed for land ice, particularly from the Greenland ice sheet, amounting to $3.0 \pm 0.3 \cdot 1000$ km^3 decade^{-1}, based on the period 2003 to 2012 (Khan et al., 2015). Earlier studies noticed statistical links between an amplified sea ice loss at high latitudes and an increased occurrence of weather extremes at mid-latitudes (Francis and Vavrus, 2012; Tang et al., 2014; Screen and Simmonds, 2013; Cohen et al., 2014). However, the robustness of these links has been questioned and the underlying mechanisms are poorly understood (Barnes, 2013; Overland et al., 2015; Blackport and Screen, 2020).

One potential connection occurs through the ocean. Specifically, the loss of sea ice and glacial ice in the Arctic and sub-Arctic regions constitutes a source of freshwater for the North Atlantic (Bamber et al., 2018; Carmack et al., 2016). Large North Atlantic freshwater anomalies, moreover, were found to give rise to cold surface anomalies and the development of storms in the subpolar region in winter (Oltmanns et al., 2020). In turn, cold anomalies in the subpolar region in winter were found to

precede heat waves over Europe in the subsequent summer (Duchez et al., 2016; Mecking et al., 2019). The heat waves were
25 attributed to a stationary jet stream over the North Atlantic (Duchez et al., 2016) and were successfully reproduced in model
simulations initialised with the cold anomaly (Mecking et al., 2019). Thus, by triggering cold anomalies in winter, increased
surface freshening could initiate a deterministic chain of events that first leads to cold anomalies and storms in winter and then
heat waves in the subsequent summer.

While earlier studies support individual connections between the North Atlantic sea surface temperature (SST) and the jet
30 stream (Woollings et al., 2010), or between shifts in the jet stream and European heat waves (Dong et al., 2013; Gervais et al.,
2020), the role of freshwater in initiating this causal chain is unclear. Yet, given that the Arctic and sub-Arctic regions are
expected to continue to warm and release freshwater from melting sea ice and glacial ice into the North Atlantic, it is critical
to understand how the resulting feedbacks will affect weather in Europe.

Despite the expected increased freshwater fluxes into the North Atlantic in future, their potential influences on European
35 summer weather have not been investigated. A major challenge associated with the analysis of freshwater anomalies arises
from the difficulty to observe and simulate salinity. Freshwater is advected into the subpolar region through mesoscale eddies
requiring a high resolution of ∼1/12° (Marzocchi et al., 2015; Böning et al., 2016; Müller et al., 2019). Most current coupled
global climate models have a coarser resolution, giving rise to salinity biases (Mecking et al., 2017; Menary et al., 2015; Wu
et al., 2018). Moreover, in-situ observations of sea surface salinity mostly stem from Argo floats and cannot capture the high
40 spatial variability at high temporal resolution. Lastly, satellite observations of sea surface salinity are associated with large
uncertainties and only available since 2009 (Bao et al., 2019; Xie et al., 2019).

Given the limitations associated with the currently available model and observational products of sea surface salinity, we
use a new approach to estimate freshwater variations, taking advantage of a dynamical constraint of the sea surface salinity
on the SST: In the subpolar region in winter, the air is colder than the ocean surface. Thus, the surface water is cooled by the
45 air, becomes denser, and sinks. Enhanced surface freshening reduces the density and thus requires additional cooling before
the surface water is dense enough to be mixed down. Under certain conditions, this constraint of freshwater on the SST can be
exploited to infer its variability using a mass balance analysis (Oltmanns et al., 2020).

In the following, we describe the data and model products (Section 2) and explain the approach to estimate freshwater
variability from a surface mass balance (Section 3). We then examine ocean-atmosphere feedbacks initiated by freshwater
50 anomalies and demonstrate their links with European summer weather based on regression and composite analyses (Section
4). We conclude by evaluating the results of the multifaceted analyses and discussing their implications (Section 5).

2 Data

To examine the ocean atmosphere feedbacks associated with freshwater anomalies, we focussed on the period since 1979,
motivated by the increased data quality associated with the onset of satellite observations in 1979. This provides us with a
55 well-observed period of over 40 years. Next, we describe the data products involved in this study and explain the method that
we used to remove the warming effect of increasing greenhouse gas concentrations from the air temperature.

2.1 Observations

The analysis of ocean variability includes optimal-interpolated, remote sensing-based SST data from NOAA since 1982 (Reynolds et al., 2002) and gridded, absolute dynamic topography data since 1993, derived from altimetry, and distributed by the Copernicus Marine Environment Monitoring Service (Le Traon et al., 1998). Absolute dynamic topography represents the sea level anomaly with respect to the geoid and thus, the stream function of the geostrophic surface flow. It is used to assess changes in surface currents. To cover a notable freshwater event in 1980, we extended the NOAA SST data backward with Hadley Centre HadISST1 data since 1979 (Rayner et al., 2003; Hurrell et al., 2008). We also included hydrographic observations from a mixed-layer database derived from Argo float profiles (Holte et al., 2017), and raw profiles to compare freshwater anomalies, estimated from the mass balance analysis, with in-situ observations.

The ocean data is complemented by output from the ERA5 atmospheric reanalysis model from the European Centre for Medium-Range Weather Forecasts since 1979 (Hersbach et al., 2018). In addition to the standard variables from ERA5, we estimated the maximum Eady growth rate. The maximum Eady growth rate is used to assess the baroclinic instability in the atmosphere over increased meridional SST gradients. Following earlier studies (Lindzen and Farrell, 1980; Dierer et al., 2005), we estimated the maximum Eady growth rate in the 1000 hPa to 750 hPa layer with $\sigma_E \approx 0.31 \frac{f}{N} \mid \frac{u_{750} - u_{1000}}{z_{750} - z_{1000}} \mid$, where f is the Coriolis frequency, u is the zonal wind, z the height, N the Brunt-Väisälä frequency and the subscripts refer to the associated pressure levels.

A key parameter, used to derive freshwater indices, is the mean North Atlantic Oscillation (NAO) in summer, obtained from the National Oceanic and Atmospheric Administration (NOAA) Climate Prediction Center. The NAO index was calculated using Rotated Principal Component Analysis, applied to the monthly standardised 500 hPa geopotential height anomalies between 20°N and 90°N (Barnston and Livezey, 1987) and identified as the dominant mode of variability in the northern hemisphere. A detailed derivation can be found at https://www.cpc.ncep.noaa.gov/products/precip/CWlink/pna/nao.shtml.

2.2 Model simulations

To investigate the role of the SST in driving the atmospheric circulation, we employed SST-forced simulations from ECHAM5 (Roeckner et al., 2003) and CAM5 (Neale et al., 2012), obtained from the Facility of Climate Assessments repository (Murray et al., 2020). The simulations were performed with the prescribed, observed SST and sea ice cover and time varying greenhouse gases and ozone. Further details on the experimental setup can be obtained from https://psl.noaa.gov/repository/entry/show?entryid=85181601-0435-40be-8461-e282ac884144. ECHAM5 was run with a horizontal resolution of 0.75° x 0.75°, 31 vertical levels and 50 ensemble members, and CAM5 was run with a horizontal resolution of 1° x 1°, 30 vertical levels and 40 ensemble members. We excluded other models from the repository that do not cover the period 1979–2018 or that do not include all investigated parameters.

2.3 Removing greenhouse gas effects

Since the freshening of the subpolar North Atlantic exhibited a trend over the recent period (Tesdal et al., 2018), trends are part of the signal we are interested in. However, the recent period was also characterised by a significant trend of increasing

90 greenhouse gas concentrations, implying that the warming trend resulting from increased greenhouse gases could potentially superimpose on a warming trend due to freshwater events and distort their effect on European air temperatures.

To reduce the influence of increasing greenhouse gas concentrations on European air temperatures, we subtracted regionally averaged trends from the air temperature, both in ERA5 and the model simulations. By using regional averages, we assumed that the trend of the direct, greenhouse gas-induced warming over Europe is distributed relatively uniformly. On the other

95 hand, a potential additional warming trend over Europe due to shifts in the jet stream must be balanced by a cooling trend at neighbouring locations, particularly over the North Atlantic, since the warming and cooling signals would be linked to the same baroclinic instability in the atmosphere.

We tested different regions and found that the results are not sensitive to the area that is used for the averaging, as long as it is sufficiently large. Here, we averaged over the main area of investigation from 25 °N to 65 °N and from 60 °W to 60 °E,

100 resulting in an average trend of ~ 0.03 °C year^{-1} in the 2-m air temperature from ERA5. Extending the region in any direction does not appreciably change this trend, nor the subsequent results, consistent with the assumption that the direct warming trend that is solely due to increasing greenhouse gases is distributed relatively uniformly.

While the summer air temperature is strongly affected by a spatially uniform warming trend, the other variables exhibit no or only minor trends after they have been averaged over a large area. Thus, when we remove the trend in the air temperature

105 prior to the analyses, we obtain a signal that is dynamically consistent across all investigated variables. If, on the other hand, we do not remove the trend in the air temperature, we still obtain the same patterns throughout the results but there would be a large-scale, uniform warming signal superimposed over the full domain.

We did not remove a trend from the SST since the SST is used to estimate freshwater anomalies. Thus, any processing of the SST variability may lead to inconsistencies with the surface heat fluxes in the mass balance analysis. Instead — to avoid that a

110 potential, greenhouse-gas induced warming trend interferes with freshwater-linked SST signals — we only considered spatial gradients in the SST throughout the dynamical analyses. Spatial SST gradients are dynamically of most interest, and remain, by construction, unaffected by any spatially uniform, greenhouse gas-induced warming trends.

3 Estimation of freshwater anomalies

The objective of this study is to investigate feedbacks initiated by freshwater anomalies. However, high-quality global salinity

115 measurements have only been routinely available since 2002, and mostly in the open ocean from Argo floats. Moreover, satellite observations of the sea surface salinity are of relatively low accuracy and only available since 2009 (Bao et al., 2019; Xie et al., 2019). Considering the limitations associated with currently available salinity products, we construct indices that (1) allow to estimate the variability of freshwater from a surface mass balance, and (2) are highly correlated with the obtained freshwater estimates. In the following, we describe the key steps while a detailed derivation of the indices is provided in Appendix A.

3.1 Mass balance

We start with a surface mass balance to obtain an estimate of the mixed layer density in response to external drivers (Fig. 1):

$$\int_{-h(t)}^{0} \frac{\partial \rho}{\partial t}\, dz = -\frac{B}{g} + A + M, \tag{1}$$

where ρ is the density, h is the mixed layer depth, A corresponds to horizontal mass transports, g is the gravitational acceleration, B is the buoyancy flux through the surface, and M is the mass flux through the base of the mixed layer (Gill, 2016). Next, we linearise the equation of state $\partial \rho \approx \rho_0 \left(\alpha \partial T + \beta \partial S \right)$, where T is the temperature, S is the salinity and α and β are the thermal and haline expansion coefficients. Thus, we arrive at an equation that relates mixed layer temperature and salinity changes on the lefthand side to the drivers of density anomalies on the righthand side.
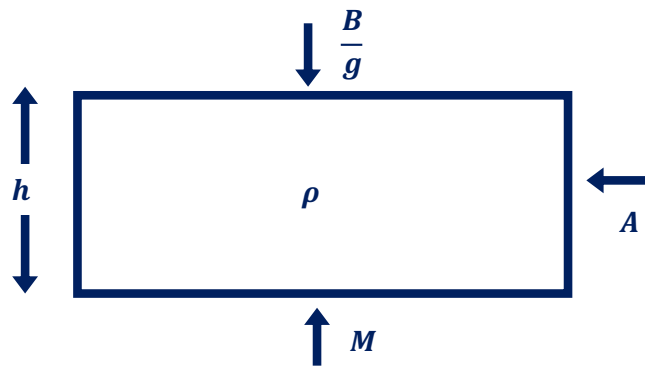

Figure 1. Mass budget for a mixed layer of depth h in a selected cold anomaly region, taking into consideration horizontal advection A, the density flux from beneath the mixed layer M, and the density contribution from the surface buoyancy flux $\frac{B}{g}$.

While salinity changes are a response in Eq. (1), they can, in turn, constrain the drivers of density anomalies on the righthand side. Large freshwater anomalies, in particular, impede downward mixing (M) and thus limit the oceanic heat release to the atmosphere (B). At the same time, a stronger surface cooling is required to mix freshwater down. Thus, when freshwater anomalies are so large that they control the mixed layer stratification, they set the temperature that the surface water is required to have before it is dense enough to be mixed down (Oltmanns et al., 2020; Stewart and Haine, 2016).

To exploit this constraint of salinity on temperature, we derive indices that exhibit a strong relationship to subpolar temperature anomalies but not to the drivers of density anomalies on the righthand side of Eq. (1). We then take advantage of these relationships by regressing Eq. (1) onto the indices. Since the drivers are (by construction) not connected to the indices, they drop out after the regression such that the density changes implied by the temperature anomalies must be balanced by density changes associated with salinity anomalies. In essence, the indices serve as filters that select conditions in which stratification has been controlled by salinity, allowing us, under these conditions, to infer the variability of freshwater from the SST.

3.2 Derivation of freshwater indices

140 To derive suitable indices for freshwater anomalies, we started with the NAO in summer and then subsampled this index to obtain indices that show a strong linear relationship with the subpolar SST in the subsequent winter. The choice of the summer NAO was motivated by previous studies suggesting that the NAO is physically connected to drivers of freshwater anomalies in the North Atlantic, such as melting and runoff from Greenland (Hanna et al., 2013, 2021), or changes in the subpolar gyre circulation (Häkkinen and Rhines, 2009; Häkkinen et al., 2011, 2013; Holliday et al., 2020). However, in this study we do not

145 further investigate the physical drivers of freshwater anomalies nor their connections to the indices. We only take advantage of the statistical links between the indices and the freshwater anomalies.

In summary, the freshwater indices fulfil two tasks: (1) they allow us to estimate freshwater anomalies from a surface mass balance, and (2) they are highly correlated with the resulting freshwater estimates. The freshwater anomalies are not known a priori but are obtained through the indices. In turn, these tasks require that the indices have a close relationship with the North

150 Atlantic SST anomalies in winter, which is achieved by subsampling the summer NAO.

We tested different strategies for the subsampling, for instance by randomly selecting years, by manually removing outliers, or by not applying any subsampling at all. In each case, we found that the strength of the correlations between the (subsampled) index and the resulting freshwater anomalies is carried forward: The better the index represents the initial freshwater anomalies, the stronger are also its links with the subsequent ocean-atmosphere evolution. All details of the subsampling and evaluation

155 of the mass balances are provided in Appendix A.

After the subsampling, we obtain two freshwater indices, F_E and F_W, that exhibit a close relationship with the North Atlantic SST in the subsequent winter (Fig. 2a-c), characterised by steep regression slopes and high correlations of ∼0.98 and ∼0.90 respectively (Fig. 2d). Higher indices are associated with a colder subpolar region and a warmer subtropical region, amplifying the meridional SST gradient. As a result of the steep regression slopes, evaluation of the surface mass balance allows us to

160 estimate the associated freshwater anomalies with an uncertainty of less than 4% for F_E years and less than 7% of F_W years. Freshwater anomalies associated with the F_E subset are strongest over the eastern subpolar region (Fig. 3a), while freshwater anomalies associated with the F_W subset also extend over the western subpolar region (Fig. 3b).

Another implicit advantage of the approach is that both indices are highly correlated with freshwater anomalies in the subsequent winter, with the correlations exceeding 0.9 over large parts of the subpolar region (Fig 3c and d). While the choice of the

165 two indices is thus motivated by their strong links to freshwater anomalies, the focus of this study is on the link between freshwater anomalies and their downstream effects. High correlations between the indices and the subsequent freshwater anomalies are a prerequisite, not a conclusion, and we make no assumptions on the suitability of both indices outside the investigated subsets.

Without the additional subsampling, we would still obtain significant freshwater anomalies in the subpolar region but the

170 uncertainty of the estimated freshwater anomalies would increase to ∼10%, and their correlation with the index would decrease. As a result of the reduced correlations and accuracy, the index would be less suitable to represent freshwater anomalies and less satisfactory to assess their impacts, which are investigated next.
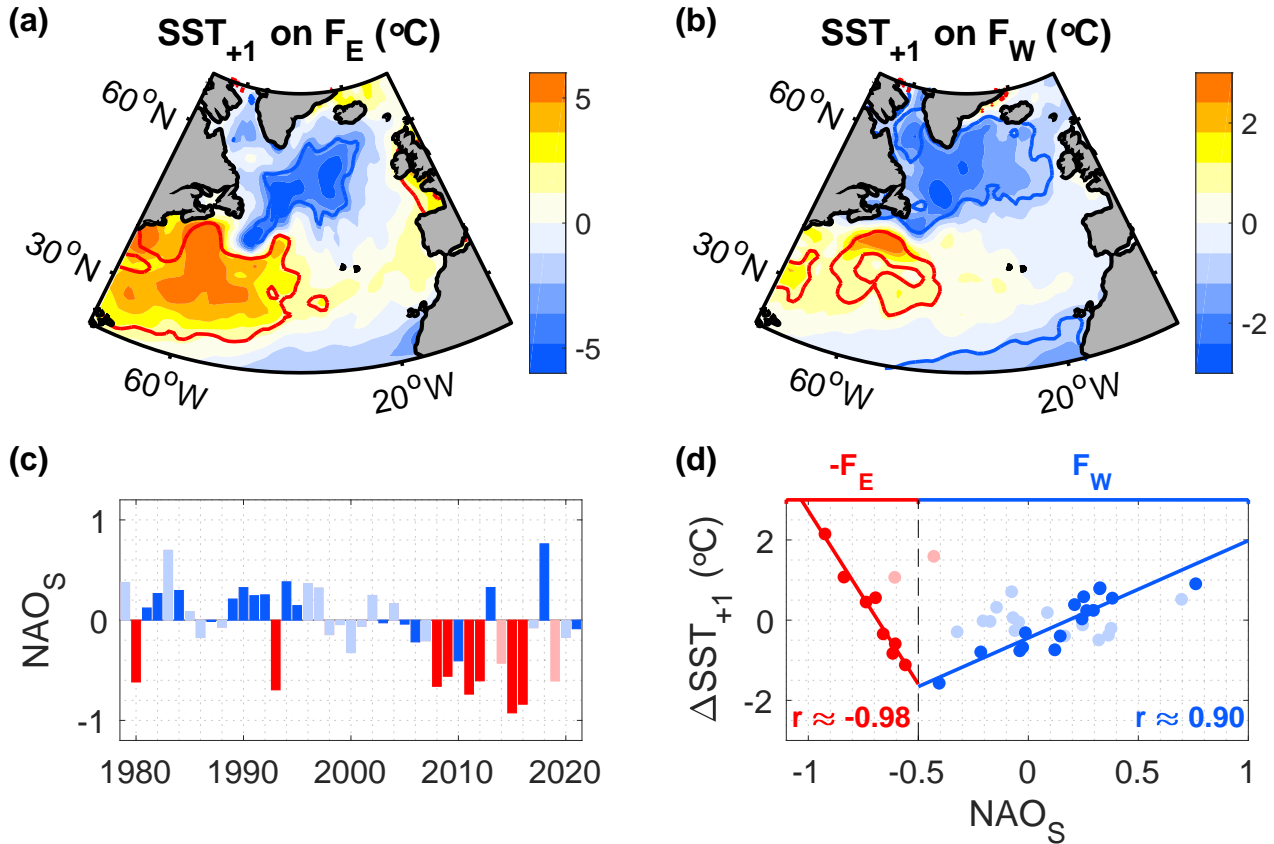
Figure 2. (a,b) Regression of the SST in winter (January through to March) onto the two freshwater indices (a) F_E and (b) F_W, obtained by subsampling the NAO index from the preceding summer (Appendix A). The corresponding years are shown by the strong red and blue colours in panels c and d, excluding the more transparent years. Thus, F_E includes 8 years while the regression on F_W is based on 16 years. Contours encompass regions that are significant at the 95% confidence level. The '+1' in the title refers to the time lag of the SST signal since it appears in the winter after the summer index. (c) Variability of the NAO index in July and August (NAO_S), with the colour coding matching that in d. (d) Relationship between NAO_S and the subsequent winter SST, where ΔSST corresponds to the SST difference between the red and blue 95% confidence regions in panels a (red years) and b (blue years) respectively, relative to the climatological mean.
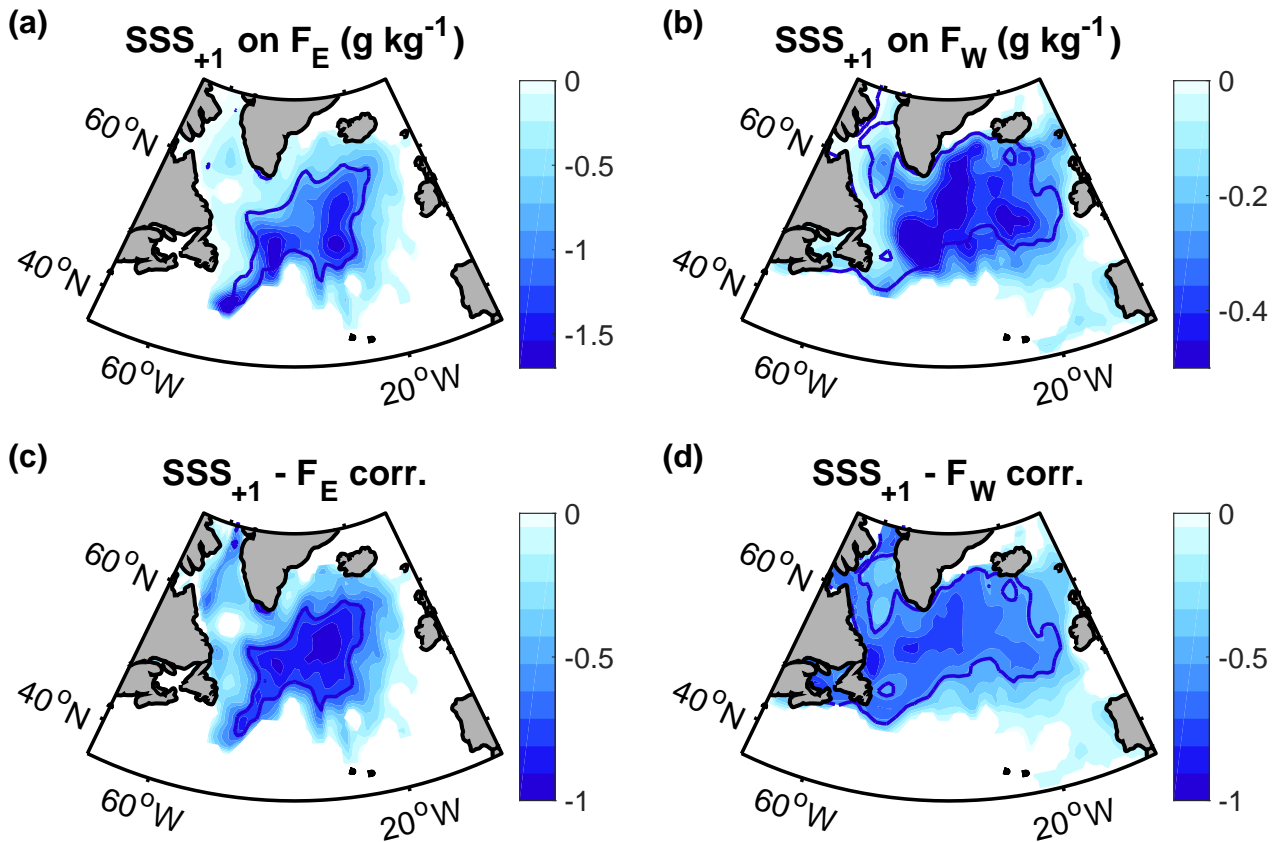
Figure 3. (a,b) Regression of the sea surface salinity in winter (January through to March) on the two freshwater indices from the preceding summer, obtained by subsampling the summer NAO (Fig. 2). The contours delineate the regions that are significant at the 95% confidence level. (c,d) Correlations between the sea surface salinity in winter and the freshwater indices from the preceding summer, with the thick contours delineating the regions that are significant at the 95% confidence level, assessed by means of two-sided t-tests.

4 Results

Taking advantage of the close relationships between the freshwater anomalies and their indices, we next examine the evolution
175 of freshwater anomalies based on linear regressions and assess potential links to European summer weather. The regression
analyses will be complemented by model simulations to evaluate the role of freshwater-induced SST patterns for the occurrence
of heatwaves and droughts over Europe. We will further explore the link between freshwater anomalies in the subpolar North
Atlantic and heat waves over Europe by starting from European summer weather. Specifically, we will construct composites
of the ocean and atmospheric conditions associated with the 10 warmest and coldest European summers over the last 40 years,
180 compare the preceding freshwater anomalies, and assess whether they were significantly different from each other.

Weather and
Climate Dynamics
Discussions

Open Access

EGU

4.1 Atmosphere-ocean feedbacks in winter

We start by examining the evolution of freshwater anomalies in winter. We focus on the anomalies that are represented by the F_E subset (Fig. 3a) due to their sharper SST signals. However, freshwater anomalies associated with the F_W subset show qualitatively the same atmospheric responses, both in winter (not shown) and in summer (Section 4.2).

185   Since the meridional SST gradient is increased in winters after stronger freshwater anomalies, there is a sharper SST front between the North Atlantic Current and the subpolar gyre (Fig. 2a). Directly above this sharper SST front, we observe an amplified baroclinic instability in the atmosphere, indicated by an enhanced Eady growth rate (Fig. 4a).
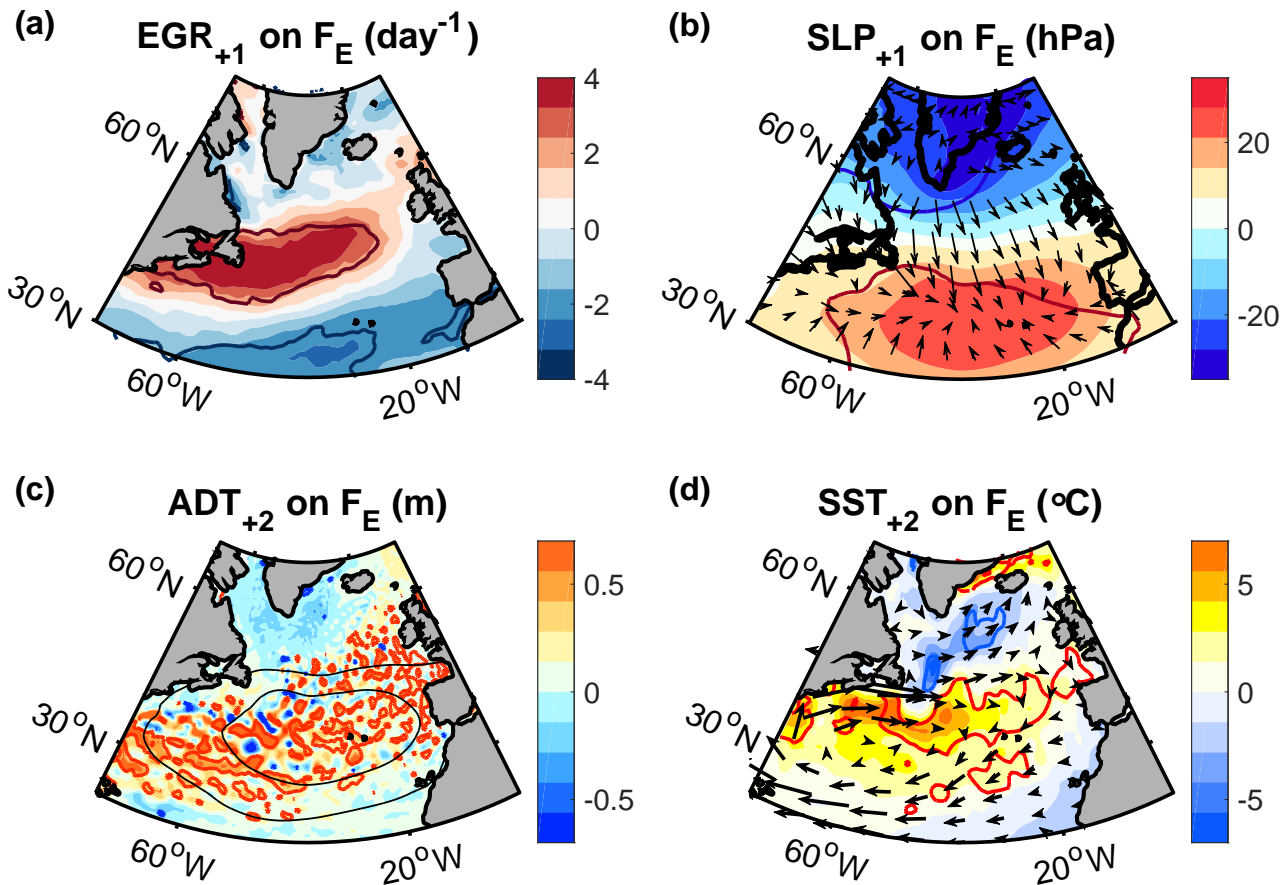

Figure 4. Regressions of (a) the maximum Eady growth rate, (b) the sea level pressure, (c) the absolute dynamic topography (ADT) and (d) the SST in winter (January through to March) on F_E, based on 8 winters (Fig. 2c). (a) and (b) are in the first winter after the events whereas (c) and (d) are in the second winter after F_E (indicated by the '+1' and '+2' in the title). The arrows in (b) show the direction of the associated Ekman transports. The arrows in (d) represent the smoothed geostrophic flow implied by the ADT anomaly. The thin black contours in (c) show the region of Ekman flow convergence from (b). Thick contours in all panels delineate the 95% confidence regions.

The amplified baroclinic instability manifests itself in a distinct circulation anomaly. When an air parcel travels northward across an anomalously sharp SST front, it rises because it is warmer than the surrounding air masses. By rising, the air column

190 stretches, acquiring positive vorticity. The opposite occurs when an air parcel travels southward across the front. Thus, the sharper SST front is expected to lead to an enhanced baroclinic wave activity with stronger zonal winds, implying an increased poleward transfer of westerly momentum flux (O'Reilly et al., 2017; Omrani et al., 2019).

The increased poleward momentum transfer is confirmed by the observations after freshwater anomalies, and reflected in a cyclonic anomaly north of the front and an anticyclonic anomaly to the south (Fig. 4b), consistent with the theoretical response

195 to the underlying SST front. While a detailed investigation of the associated diagnostics is beyond the scope of this study, the large-scale atmospheric circulation anomalies are also reproduced by SST-forced model simulations, albeit at lower amplitudes, supporting that the ocean significantly contributes to these anomalies (Appendix B).

The obtained atmospheric circulation anomaly drives a convergent Ekman transport between the subtropical and subpolar gyre (Fig. 4b), leading to an increase in sea level. The increased sea level and associated ocean instabilities are manifest in a

200 broad band of anti-cyclonic eddies that extends into the second winter after the events (Fig. 4c). The eddies are not visible in the SST due to the coarser $1°$ x $1°$ resolution of the SST product, compared to the $0.25°$ x $0.25°$ resolution of the absolute dynamic topography product.

The integrated effect of the anti-cyclonic eddies is a reduced geostrophic, eastward speed at the southern edge of the band and an increased geostrophic, eastward speed at its northern edge (Fig. 4d). This circulation pattern has previously been referred to

205 as inter-gyre gyre circulation (Marshall et al., 2001) and is equivalent to a northward shift of the North Atlantic Current (Kostov et al., 2021; Zhao and Johns, 2014). The northward shift, in turn, implies a warm anomaly to the south of the subpolar cold anomaly (Fig. 2a and 4d). Thus, the ocean and atmospheric circulation anomalies are reinforcing each other, and the overall effect of the air-sea coupling is an increased SST front between the warm, northward-shifted North Atlantic Current and the cold subpolar gyre, representative of the North Atlantic SST tripole pattern (Czaja and Frankignoul, 2002).

210 The northward current shift, revealed by the altimetry observations, is seen in both the first, and the second winter after freshwater events. However, in the first winter after the events, the northward shift of the North Atlantic Current is obscured in the SST over the eastern North Atlantic (Fig. 2a). Only in the second winter, the northward current shift is revealed through a warm anomaly all across to the eastern boundary of the North Atlantic (Fig. 4d).

We summarise that freshwater anomalies are linked to cold anomalies in the subpolar region in winter (Figs. 2 and 3). The

215 cold anomalies lead to an enhanced meridional SST gradient, implying a sharper SST front between the subpolar gyre and the subtropical gyre. The sharper SST front is associated with an amplified baroclinic instability in the atmosphere (Fig. 4a) that is characterised by a more cyclonic circulation anomaly over the subpolar gyre and a more anticyclonic anomaly to the south (Fig. 4b). This circulation anomaly drives a convergent Ekman transport in the inter-gyre region (Fig. 4b), resulting in elevated sea level (Fig. 4c). The associated geostrophic surface flow implies a northward shift of the North Atlantic Current and, in turn,

220 a warm anomaly to the south of the cold anomaly (Fig. 4d). Thus, the warm anomaly further increases the meridional SST gradient and reinforces the positive air-sea feedback. While this mechanism has been demonstrated using the F_E subset, the signals for the F_W subset are qualitatively the same.

4.2 Implications for European summer weather

The preceding analysis revealed a close link between the magnitude of freshwater anomalies and subsequent winter conditions.
225 Next, we investigate the SST and atmospheric conditions in subsequent summers. In the first summer after stronger freshwater anomalies (again represented by F_E), we find that the SST is characterised by an enhanced meridional SST gradient associated with the subpolar cold anomaly, covering part of the North Atlantic Current (Fig. 5a). In the second summer, the northward shift of the North Atlantic Current is the most pronounced signal, implying that the region of the enhanced meridional SST gradient is shifted northward compared to the first summer (Fig. 5b).

230 As in the preceding winters, the SST fronts destabilise the overlying atmosphere, resulting in an enhanced jet stream along the front (Fig. 5a and b). If the jet stream crosses the European coastline at a more northerly location, it transports less moist, maritime air masses from the North Atlantic over the regions further to the south. Thus, in line with the more northerly SST front and jet stream locations (Fig. 5c and d), we observe relatively warmer and drier air over southwest Europe in the first summer after stronger freshwater events, and relatively warmer and drier air over northwest Europe in the second summer (Fig.
235 5e-h).

Similar to the F_E freshwater anomalies, the freshwater anomalies associated with the F_W subset are also characterised by a cold anomaly in the subsequent summer. However, compared to F_E freshwater anomalies, the F_W freshwater anomalies are followed by a more confined cold anomaly over the central North Atlantic in summer, with the regressions peaking in July and August (Fig. 6a). Consequently, we observe a sharp northward deflection of the jet stream (Fig. 6b), leading to more westerly
240 warm and dry anomalies over Europe (Fig. 6c and d).

Despite these individual differences, the overall patterns are similar after F_E and F_W freshwater anomalies: Both types of freshwater anomalies are characterised by a cold anomaly and northward deflection of the jet stream around the cold anomaly over the North Atlantic in the subsequent summer. In both cases, the northward deflection of the jet stream reduces the advection of moist, maritime air masses over large parts of Europe, resulting in warmer and drier weather.

4.3 Predictability of European summer weather
245

The preceding analyses demonstrate a significant link between North Atlantic freshwater anomalies and European summer weather in subsequent years. This raises the question to what extent this link can be exploited to predict European summer weather in advance. Since most current coupled global climate models have large freshwater biases, they are not suitable to estimate the predictability arising from freshwater. Thus, we first assess the predictability based on the explained variance in
250 the observations, estimated by means of the squared correlation coefficient.

The variance of the near surface temperature and precipitation minus evaporation anomalies, explained by the F_E subset, reaches and even exceeds 80% over large parts of Europe (Fig. 7a-d). For the F_W subset, the explained variance drops to ∼50% (Fig. 7e and f), as expected from the reduced correlation between the F_W index and the corresponding freshwater anomalies. In both cases, the explained variance is largest in the regions that show the strongest links with the temperature and precipitation
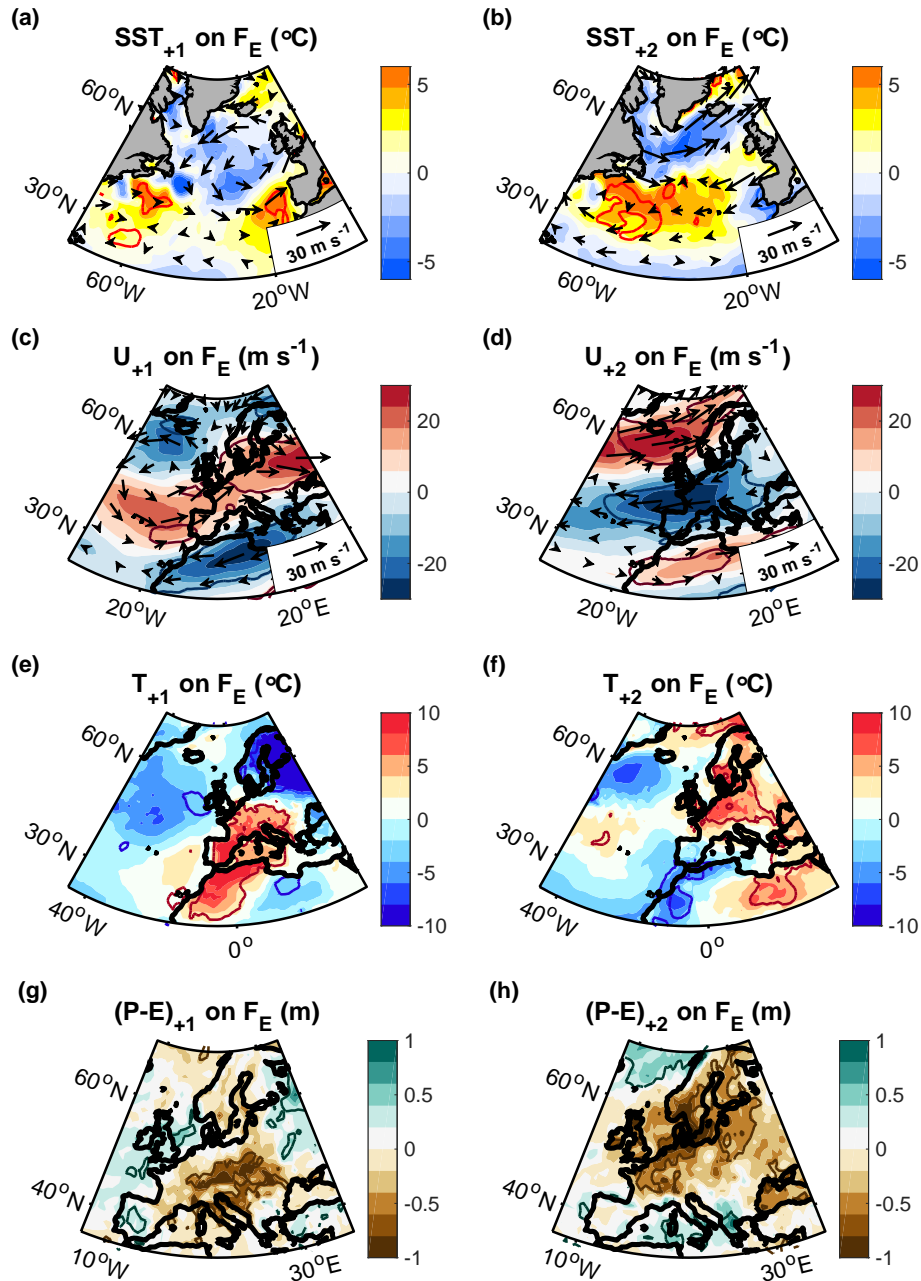255 minus evaporation anomalies (Figs. 5 and 6).

Figure 5. Regressions of (a,b) the SST with the 700-hPa winds, (c,d) the zonal winds at 700 hPa, (e,f) the 2-m air temperature and (g,h) the accumulated precipitation minus evaporation on F_E in (a,c,e,g) the first and (b,d,f,h) the second summer (May through August) after the freshwater events (indicated by the '+1' and '+2' in the titles). We removed large-scale trends from the air temperature to reduce the direct warming effect of greenhouse gases (Section 2), and we excluded the event in 2015 since its responses were covered by the 2016 event (not shown). Thick contours encompass regions that are significant at the 95% confidence level.
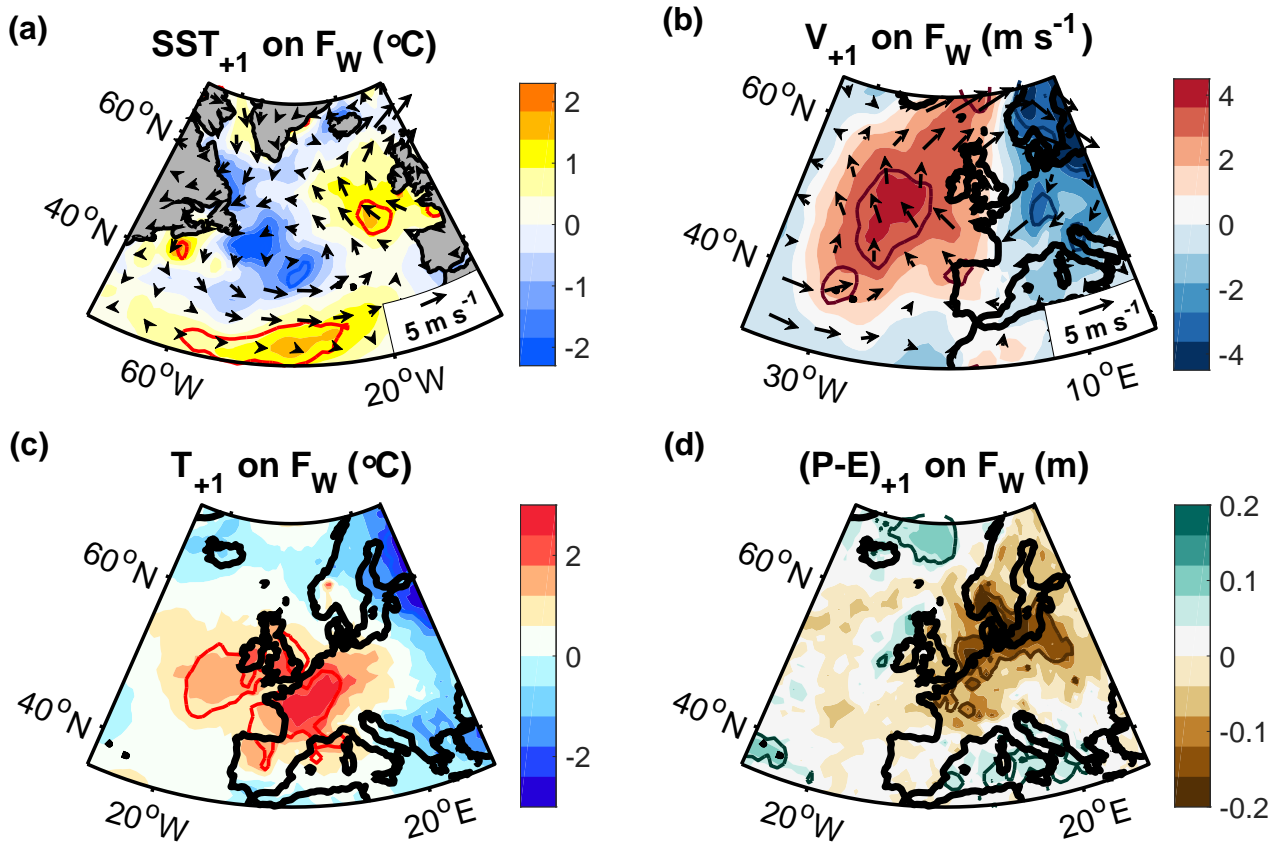
Figure 6. Regressions of (a) the SST with the 700-hPa winds, (b) the meridional winds at 700 hPa, (c) the 2-m air temperature and (d) the precipitation minus evaporation in summer (July and August) on F_W from the preceding summer, again after subtracting large-scale trends from the air temperature (Section 2). The thick contours encompass regions that are significant at the 95% confidence level.

A disadvantage of estimating predictability from the freshwater indices is the small sample size. If, instead, we approximate the freshwater variability by the meridional SST gradient in winter as an alternative freshwater index that covers the full period of investigation (Fig. 2d), the explained variance of European summer weather would decrease to ~20% and extend over a broader area (not shown). However, the correlation of this index with the associated freshwater anomaly in winter would
260 decrease accordingly. Thus, we do not expect it to adequately capture freshwater feedbacks.

Overall, we find: The higher the correlation is between the initial freshwater anomaly and its index, the higher is also the variance of European summer weather that the index subsequently explains. The F_E index, in particular, has an extremely high correlation with the initial freshwater anomaly of over ~0.9 (Fig. 3c) and explains over 80% of the variance of European summer weather. Notwithstanding the small sample sizes, these results indicate that accurate observations of surface freshwater
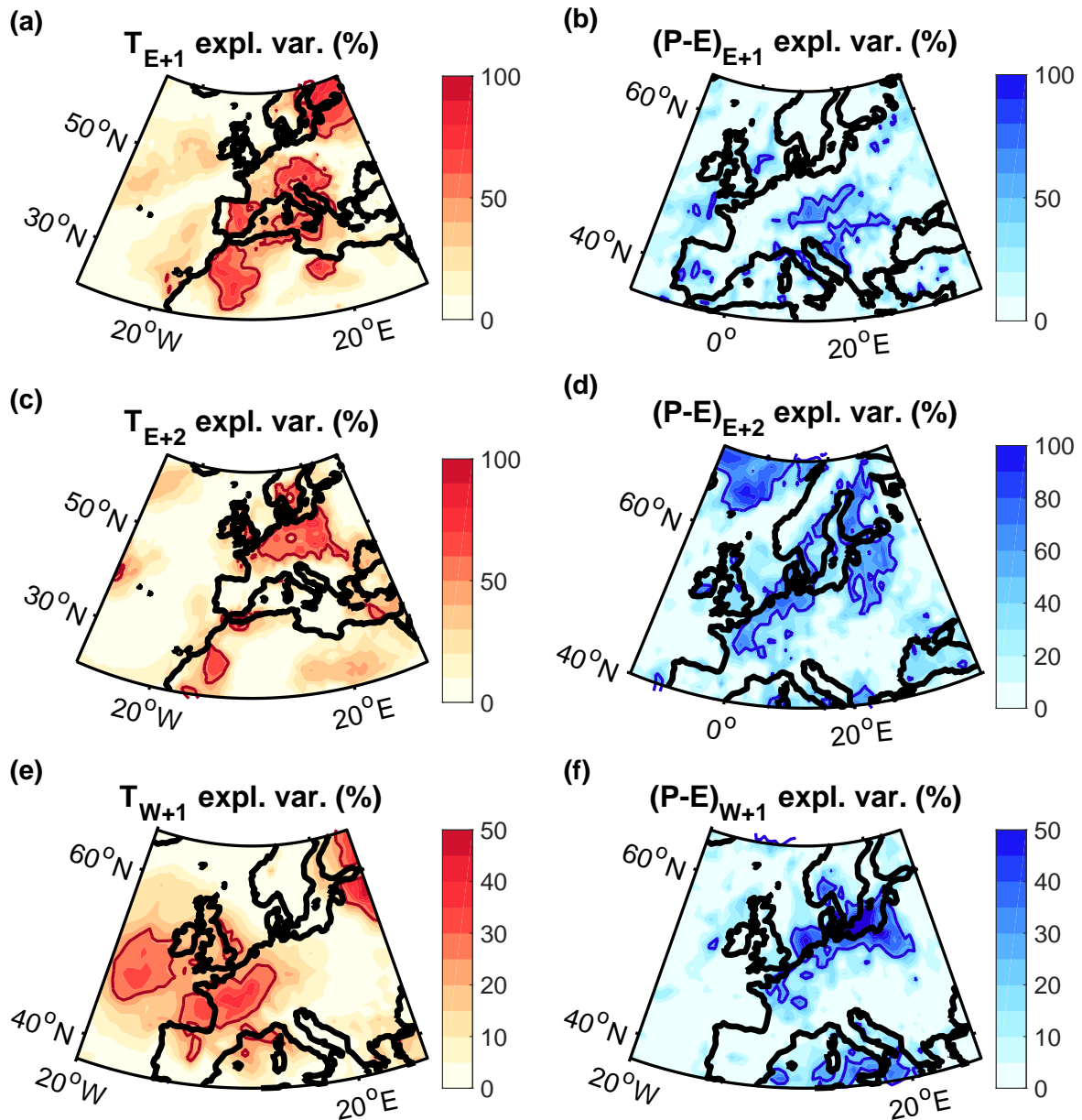265 in the subpolar region can serve as valuable constraints for seasonal to interannual weather forecasts.

13

Figure 7. Variances explained by (a-d) F_E and (e,f) F_W of (a,c,e) the 2-m air temperature and (b,d,f) precipitation minus evaporation after freshwater events. '+1' and '+2' in the titles refer to the first and second summer after the events. Thick contours delineate the regions, in which the correlation is significant at the 95% confidence level, assessed by means of two-sided Student t-tests. The explained variances were obtained from the squared correlation coefficients. Please note the different colour scales.

4.4 Simulated atmospheric response to the freshwater-induced SST

With regard to the freshwater biases in models, we do not expect models to realistically simulate potential feedbacks to freshwater anomalies. However, they may still capture the link between the characteristic SST patterns, linked to freshwater events, and the associated atmospheric response. Thus, to test the role of the SST in driving the observed atmospheric patterns, we

270 next define an SST index that captures the time variability of the spatial SST pattern linked to freshwater events (SST_{FW}). Specifically, we project the SST each summer onto the observed SST pattern after freshwater events (Fig. 8a and b). Since the objective is to demonstrate the influence of the SST, we select a time and region with a particular sharp SST gradient, which occurred over the central North Atlantic in the second summer after melt-driven events (indicated by a box in Figure 8b). The resulting pattern resembles the SST tripole pattern (Czaja and Frankignoul, 2002).

275 Next, we regress the temperature and precipitation anomalies, obtained from 90 ensemble simulations over 40 years, performed with prescribed observation-based SSTs, onto this newly-defined SST_{FW} index. We obtain a significant link between the prescribed SST pattern and the temperature and precipitation anomalies over Europe, both in the observations (Fig. 8c and e) and in the simulations (Fig. 8d and f). Overall, the observed and simulated atmospheric responses agree qualitatively well but the simulated responses are weaker and cover a larger area (Fig. 8c-f). Since the observations lie within the spread

280 of the ensemble members (Fig. 9), the differences can be reconciled by internal variability. However, the observations never lie within the interval defined by the first and third quartiles (Fig. 9). We attribute this underestimation of the obtained atmospheric anomalies to potential model biases (Osborne et al., 2020) and, more importantly, the lack of air-sea coupling in the simulations.

Selecting different times and regions does not qualitatively alter these results, as long as the resulting SST pattern include

285 a sharp SST gradient. Depending on the exact location of the SST gradient, the locations of the temperature and precipitation anomalies will shift accordingly but their overall dependence on the North Atlantic SST gradients remains.

4.5 Warm summers in Europe

The preceding analyses showed that two types of freshwater events with opposite atmospheric drivers (characterised by a high and a low summer NAO) are followed by cold anomalies over the North Atlantic in winter, shifts in the jet stream and warmer,

290 drier weather over Europe in the subsequent summers. Next, we investigate if observed warm European summers can, in turn, be linked back to a freshwater event in the preceding year.

Indeed, based on composites, we find that the 10 warmest relative to the 10 coldest summers in Europe were associated with a pronounced cold anomaly over the North Atlantic, and an atmospheric circulation anomaly that is characterised by a northward deflection of the jet stream (Fig. 10a-e). Using a surface mass balance (Appendix A), we again traced the cold anomaly back to

295 a freshwater anomaly in the preceding winter (Fig. 10f). Selecting different regions for the temperature variability over Europe shifts the location of the obtained anomalies but does not qualitatively alter these results.
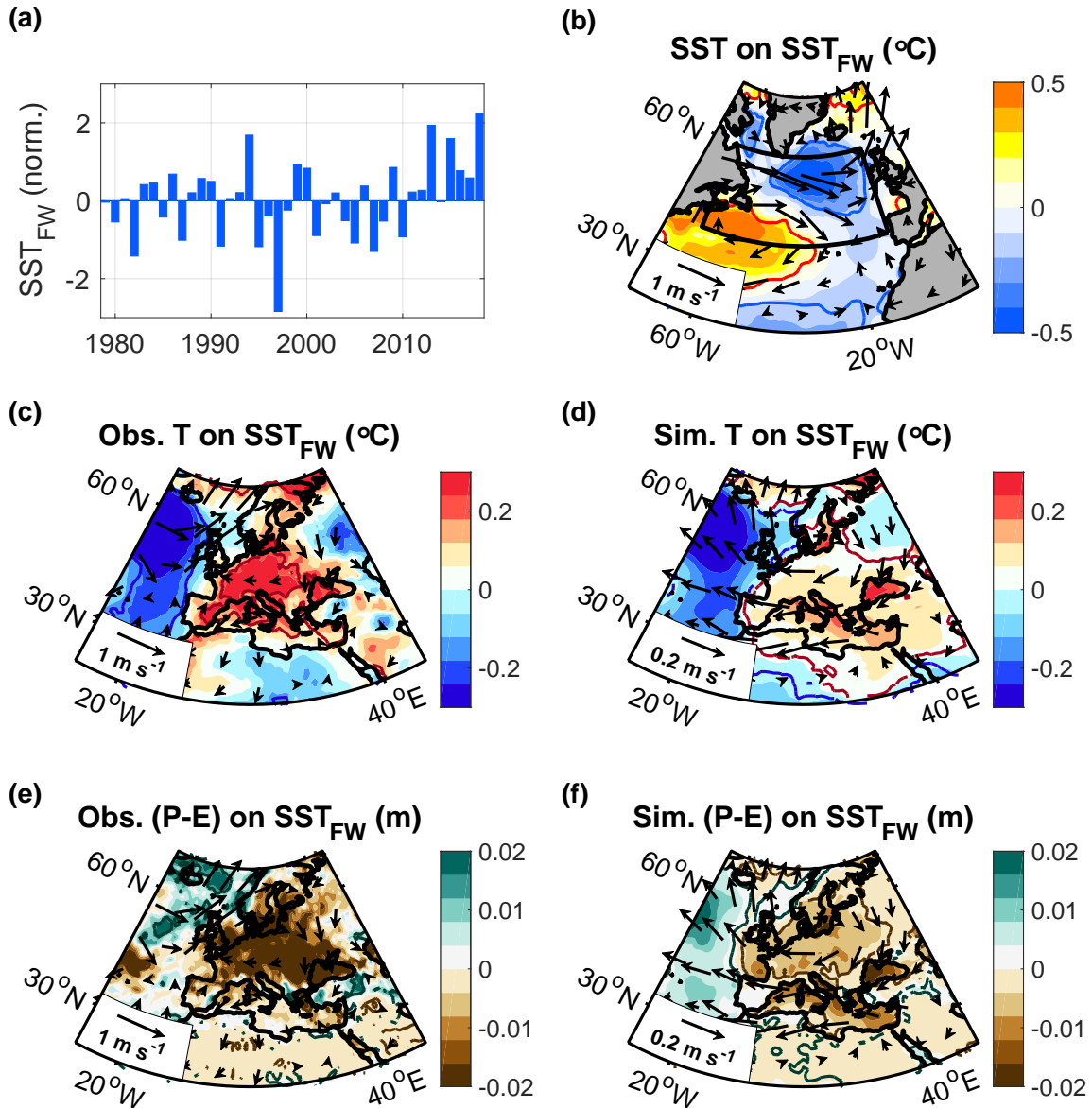
Figure 8. (a) Variability and (b) distribution of the SST pattern, linked to freshwater events, obtained by projecting the SST pattern in the box in (b) each summer (May through August) on that after freshwater events (Fig. 5b). (c,d,e,f) Regressions of (c,e) the observed and (d,f) simulated 2-m air temperature and precipitation minus evaporation in summer onto the normalised SST_{FW} index, again after subtracting the large-scale trend from the temperature. The simulations were acquired from 50 ensemble simulations from ECHAM5 and 40 ensemble simulations from CAM5 over the period 1979–2018, performed with the pre-scribed, observed SST. Shown is the mean of the regressions from the ensemble members, not the regression of the mean. Arrows indicate the observed and simulated 700 hPa winds respectively. The thick contours encompass regions that are significant at the 95% confidence level.
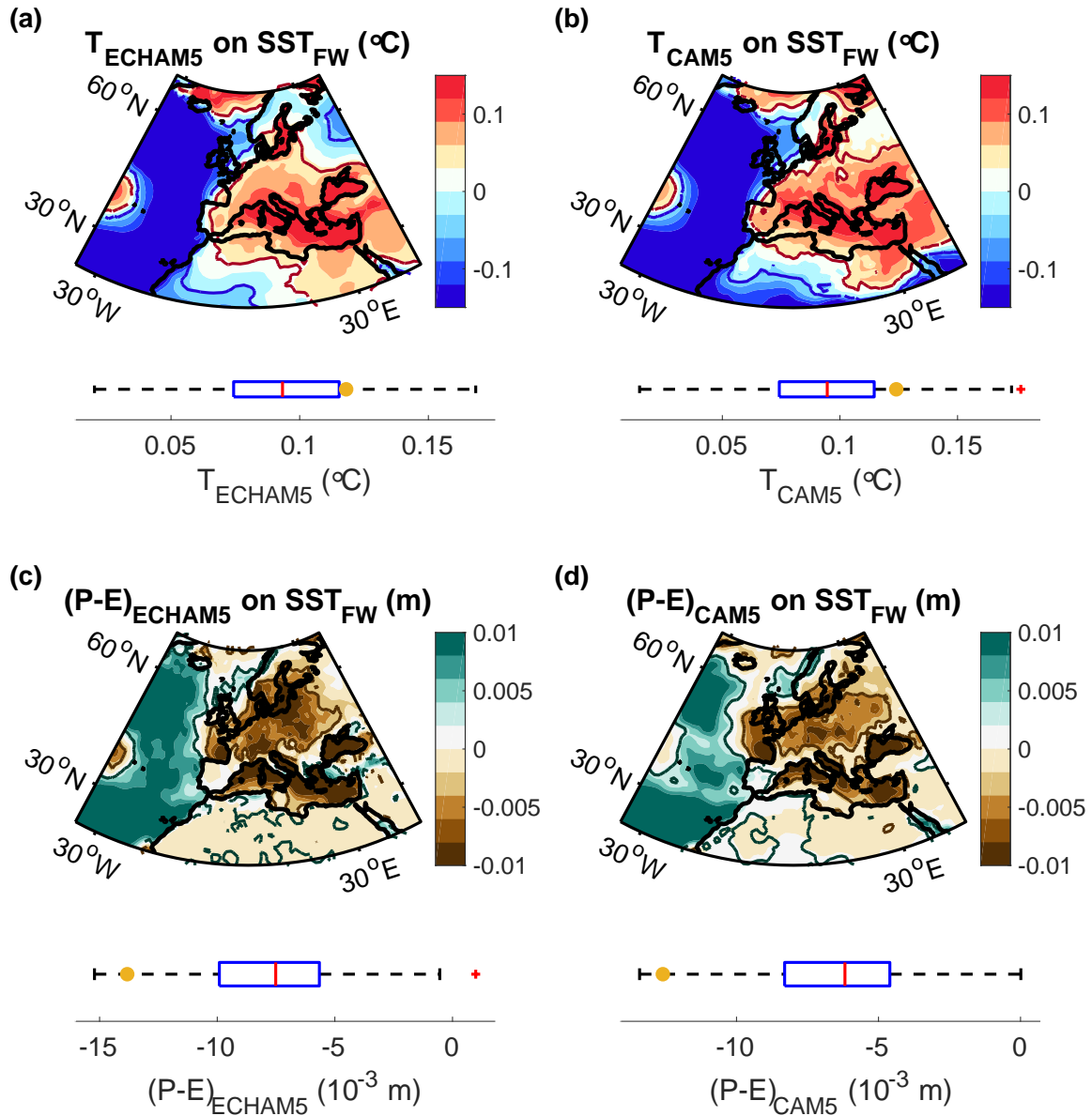
Figure 9. Regressions of (a,b) the 2-m air temperature and (c,d) the accumulated precipitation minus evaporation in summer (May through to August) on the normalised SST_{FW} pattern (Fig. 8a and b), acquired from 50 ensemble simulations from ECHAM5 and 40 ensemble simulations from CAM5 over the period 1979–2018 (as in Figure 8). Contours encompass regions significant at the 95% confidence level. The box plots show the spread of the ensemble regressions within the central red and brown 95% confidence regions respectively. On each box, the central mark indicates the median, and the left and right edges of the box indicate the 25th and 75th percentiles. The whiskers extend to the most extreme data points considering a maximum possible whisker length of 1.5 times the interquartile range. Outliers outside the maximum possible whisker length are plotted using the '+' symbol. The yellow dots represent the corresponding observed regressions.
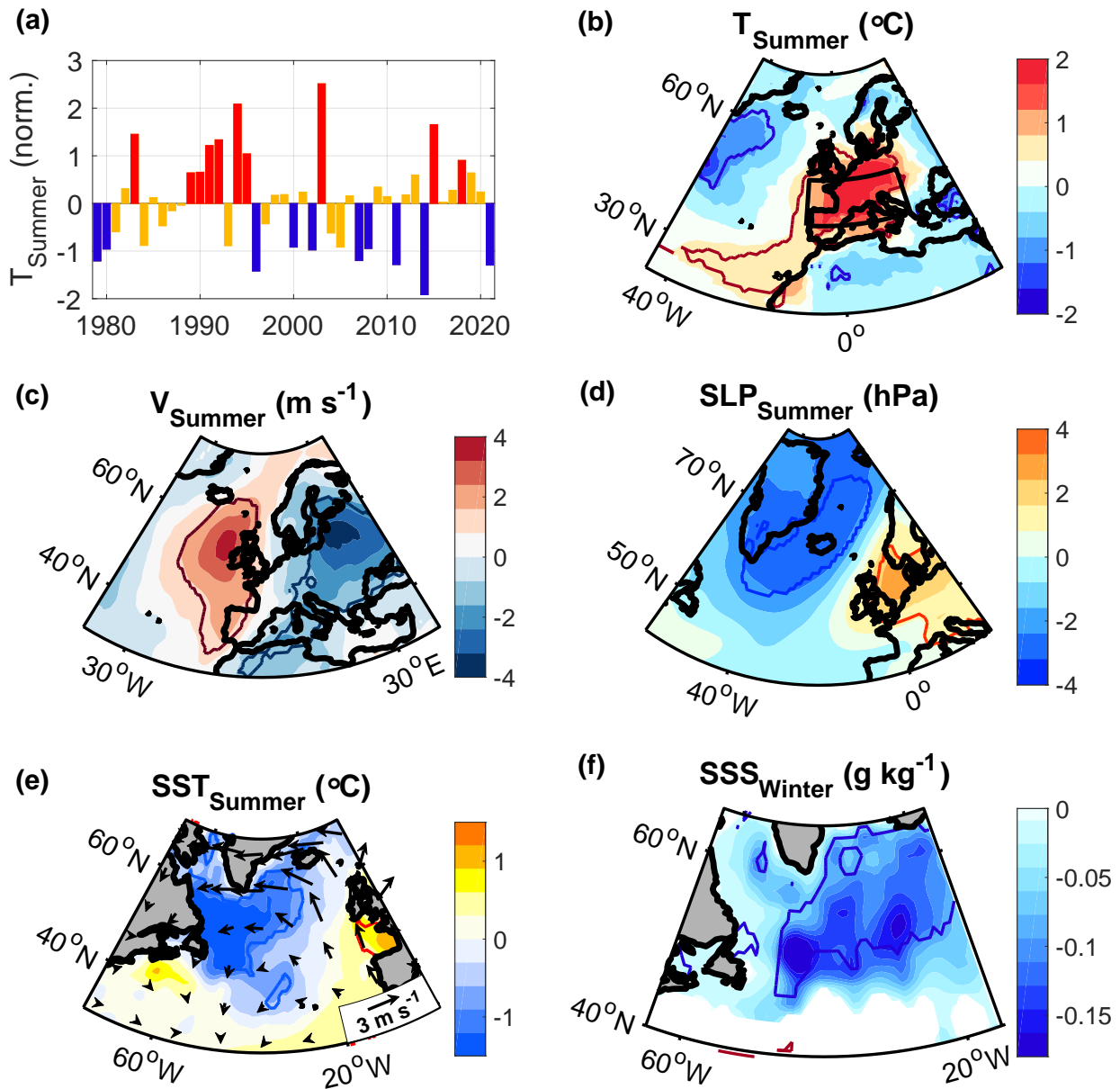
Figure 10. (a) Variability of the de-trended 2-m air temperature anomaly over land within the box shown in (b) during summer (July and August). (b,c,d,e) Composites of (b) the 2-m air temperature, (c) the meridional winds at 700 hPa, (d) the sea level pressure, and (e) the SST with the 700 hPa wind anomalies for the ten warmest minus the ten coldest summers, shown in (a). (f) Same as in (b-e) but for the sea surface salinity anomaly in the preceding winter, obtained from a surface mass balance (Appendix A). Contours delineate the regions that are significant at the 95% confidence level, assessed by means of two-sample t-tests.

5   Conclusions

This study examined the link between freshwater events in the North Atlantic and European weather in subsequent summers. Given the limitations of currently available salinity observations, we derived two freshwater indices that were obtained by es-
300 timating salinity anomalies from a surface mass balance. The indices were subsampled to be linearly correlated with subpolar freshwater anomalies. Thus, they allowed us to demonstrate the subsequent ocean atmosphere feedbacks based on linear regressions. We further supported the identified links between freshwater anomalies and subsequent European summer weather, using model simulations, forced with prescribed, observed SST, and by constructing composites of European heat waves and their preceding freshwater anomalies.

305 These multifaceted analyses reveal that enhanced freshwater anomalies are associated with cold anomalies in the subpolar North Atlantic in winter. The resulting, increased meridional SST gradient leads to an amplified atmospheric instability, which in turn feeds back on the underlying SST signal by inducing a northward shift in the North Atlantic Current. In subsequent summers, the jet stream is deflected northward over the North Atlantic, aligned with the underlying SST front, leading to warmer and drier weather over Europe.

310 The observed evolution of freshwater events follows the chain of events predicted by theory. Specifically, the link between freshwater and cold anomalies is constrained by conservation of mass. The subpolar cold anomaly increases the meridional SST gradient leading to an increased meridional temperature gradient in the lower troposphere and, in turn, an amplified baroclinic instability (Eady, 1949; Davies and Bishop, 1994). Moreover, the ocean's response to the resulting atmospheric circulation is expected from Ekman transports and geostrophy (Munk, 1950; Stommel, 1948; Vallis, 2017). Thus, these theoretical underpin-
315 nings support that the identified statistical relationships reveal a coherent, deterministic mechanism that links North Atlantic freshwater events to European summer weather.

Current numerical weather prediction systems show very limited to no forecast skill for European summer weather (Arribas et al., 2011; Dunstone et al., 2018). Thus, the existence of a significant, statistical link between North Atlantic freshwater events and European summer weather indicates new potential to enhance the predictability of European summer weather. Further
320 studies that improve the representation of North Atlantic freshwater variations in models, and that quantify the predictability arising from them, are therefore desirable. In addition, targeted observational networks that monitor the variability of freshwater anomalies may help improve current forecast systems and circumvent the use of indices in future.

Arctic sea ice and glacial ice are expected to further decline in the coming decades (Notz and Stroeve, 2018; Briner et al., 2020), increasing the freshwater discharge into the North Atlantic. With stronger freshwater events, our results imply an
325 increased risk of warm, dry European summers and of heat waves and droughts accordingly. Unfortunately, global climate models have difficulties in capturing the hydrographic structure in the subpolar North Atlantic, including the distribution of freshwater (Menary et al., 2015; Heuzé, 2017; Liu et al., 2017; Sgubin et al., 2017; Mecking et al., 2017; Wu et al., 2018). Considering the identified links between freshwater events and the subsequent ocean and atmospheric evolution, our results suggest that models may miss a key source of climate variability and potential long-range predictability.

330 *Code and data availability.* This study is only based on publicly available data and standard analysis techniques. The SST and NAO data are available from NOAA (https://psl.noaa.gov/data/gridded/data.noaa.oisst.v2.html and https://www.cpc.ncep.noaa.gov/products/precip/CWlink/pna/nao.shtml). The Hadley SST data is available from https://www.metoffice.gov.uk/hadobs/hadisst/ and a complete merged NOAA and Hadley SST product can be obtained from https://gdex.ucar.edu/dataset/158_asphilli.html. Absolute dynamic topography data is distributed by the Copernicus Marine Environment Monitoring Service (https://marine.copernicus.eu/). ERA5 data can be obtained from the European

335 Centre for Medium-Range Weather Forecasts (https://www.ecmwf.int/en/forecasts/datasets/reanalysis-datasets/era5) and the ECHAM5 and CAM5 model output can be downloaded from the Facility of Climate Assessments repository (https://psl.noaa.gov/repository/facts). Matlab codes can be obtained from the corresponding author.

Appendix A: Scale analysis of the surface mass balance

A1 Objective and approach

340 To estimate freshwater anomalies, we carry out a scale analysis of the surface mass budget for the mixed layer in the subpolar region during winter:

$$\int_{-h(t)}^{0} \frac{\partial \rho}{\partial t} \, dz = -\frac{B}{g} + A + M, \tag{A1}$$

where g is the gravitational acceleration, $h(t)$ is the mixed layer depth, A refers to horizontal mass transports, ρ is density, B is the downward buoyancy flux through the surface, and M is the mass flux through the base of the mixed layer (Fig. 1). After
345 integrating Eq. (A1) over the mixed layer, we obtain:

$$\rho_n = \frac{h_0}{h_n} \rho_0 + \left(-\frac{B_n}{g} + A_n + M_n \right) \cdot \frac{dt}{h_n}, \tag{A2}$$

with n referring to the n'th winter of an arbitrary subset of N winters and dt corresponding to the length of the winter (January through to March).

While the climatological mean mixed layer density increases during the winter, the mixed layer deepens. Thus, before the
350 winter, the mixed layer is several tens of metres deep (h_0) while during the winter, it reaches several hundred metres (h_n). Since the density anomaly in the initial shallow mixed layer becomes distributed over a much larger depth range, the first term on the righthand side is negligible compared to the other terms. Any density anomalies beneath the initial, shallow mixed layer are included in M.

Next, we linearise the equation of state around a reference state (ρ_m, S_m and T_m), which we choose to be the mean over the
355 N selected winters: $\rho_n \approx \rho_m (1 - \alpha \cdot \partial T_n + \beta \cdot \partial S_n)$, where T is the temperature, S is the salinity and α and β are the thermal and haline expansion coefficients. After plugging the linearised equation of state into Eq. (A2), we obtain a balance equation that relates temperature and salinity anomalies on the lefthand side to potential drivers of density anomalies on the righthand side of Eq. (A2).

The objective of this analysis is to find conditions (referred to as 'c'), in which the density anomaly associated with
360 temperature changes is much larger than the potential drivers on the righthand side of Eq. (A2), such that: $|\alpha \cdot \partial T_c| \gg$ $\left| \left(-\frac{B_c}{g} + A_c + M_c \right) \cdot \frac{dt}{h_c} \right|$. Under these conditions, the terms on the righthand side of Eq. (A2) drop out, implying that the temperature and salinity anomalies must compensate each other in their influence on density, and allowing us, under these conditions, to estimate the salinity anomalies from the associated temperature anomalies:

$$\beta \cdot \partial S_c \approx \alpha \cdot \partial T_c. \tag{A3}$$

365 To identify such conditions, we next derive indices that exhibit a strong relationship with subpolar temperature anomalies but not with the drivers of density anomalies on the righthand side of Eq. (A2).

A2   Derivation of freshwater indices

To identify suitable indices for freshwater anomalies, we start with the NAO in summer, which has previously been linked to potential drivers of freshwater anomalies in the subpolar North Atlantic. On the one hand, a lower NAO index in summer is associated with enhanced runoff and melting over Greenland (Hanna et al., 2013, 2021), which is a source of freshwater to the North Atlantic (Bamber et al., 2018; Dukhovskoy et al., 2019). On the other hand, a higher NAO index is associated with an intensified subpolar gyre circulation, leading to enhanced freshwater imports into the subpolar region (Häkkinen and Rhines, 2009; Häkkinen et al., 2011, 2013; Holliday et al., 2020). While the choice of the NAO index is motivated by these dynamical links, we here use it for a purely statistical purpose and make no assumptions on the dynamical underpinnings.

Consistent with the existence of multiple, possible drivers of SST and freshwater anomalies in winter, we obtain a qualitatively different relationship between the summer NAO index in July and August (NAO_S) and the SST in the subsequent winter below and above a threshold of ~ -0.5 in NAO_S. Below this threshold, there is a progressively colder subpolar SST anomaly for smaller NAO_S (Fig. A1a). Above this threshold, there is a progressively colder subpolar SST anomaly for higher NAO_S (Fig. A1b).

Next, we optimise the NAO subsets by further subsampling them. The subsampling is motivated by the objective of achieving a steep regression slope between the subsampled NAO_S index and the subsequent SST anomaly, implying that small changes in the subsampled index correspond to large changes in the subsequent SST anomaly. In turn, this high sensitivity implies that the terms on the lefthand side of Eq. (A2) become more than an order of magnitude larger than the terms on the righthand side after regressing them onto the subsampled index, allowing us to estimate the associated salinity anomalies from Eq. (A2) with higher accuracy.

For the cold anomalies associated with low values of the summer NAO (Fig. A1a), we use the subset of years in which NAO_S is less than ~ -0.5 (Fig. A1c and d). This results in a correlation of ~ 0.98 with the SST gradient in the subsequent winter ($p \approx 2.8 \cdot 10^{-5}$). We use the SST gradient rather than only the SST in the cold anomaly region because spatial gradients are more robust to local variations in the surface fluxes as well as a spatially uniform warming trend due to increasing greenhouse gases (Section 2.3).

For the cold anomalies associated with higher values of the summer NAO (Fig. A1b), the correlation with the subsequent SST gradient is weaker, amounting to ~ 0.64 ($p \approx 0.001$). Thus, to optimise our method of inferring freshwater variations from Eq. (1) and increase the accuracy of the estimated freshwater estimates, we select all years that lead to an increase in the slope of the regression line (Fig. A1d). This implies an increased sensitivity of the SST anomalies to the subsampled NAO_S. It also results in an increased correlation of ~ 0.90 ($p \approx 2.6 \cdot 10^{-6}$) between the subsampled index and the SST gradient in the subsequent winter (Fig. A1e and f).

To ensure that the results are robust, we repeated the analyses by excluding events in consecutive years. For both subsets, the results do not change noticeably if individual events are excluded, neither the winter SST, nor the subsequent ocean atmosphere evolution. This is in agreement with negligible autocorrelations across both subsets, and consistent with the scatter diagrams showing that there are no outliers or clusters of values responsible for the high correlations (Fig. A1d).
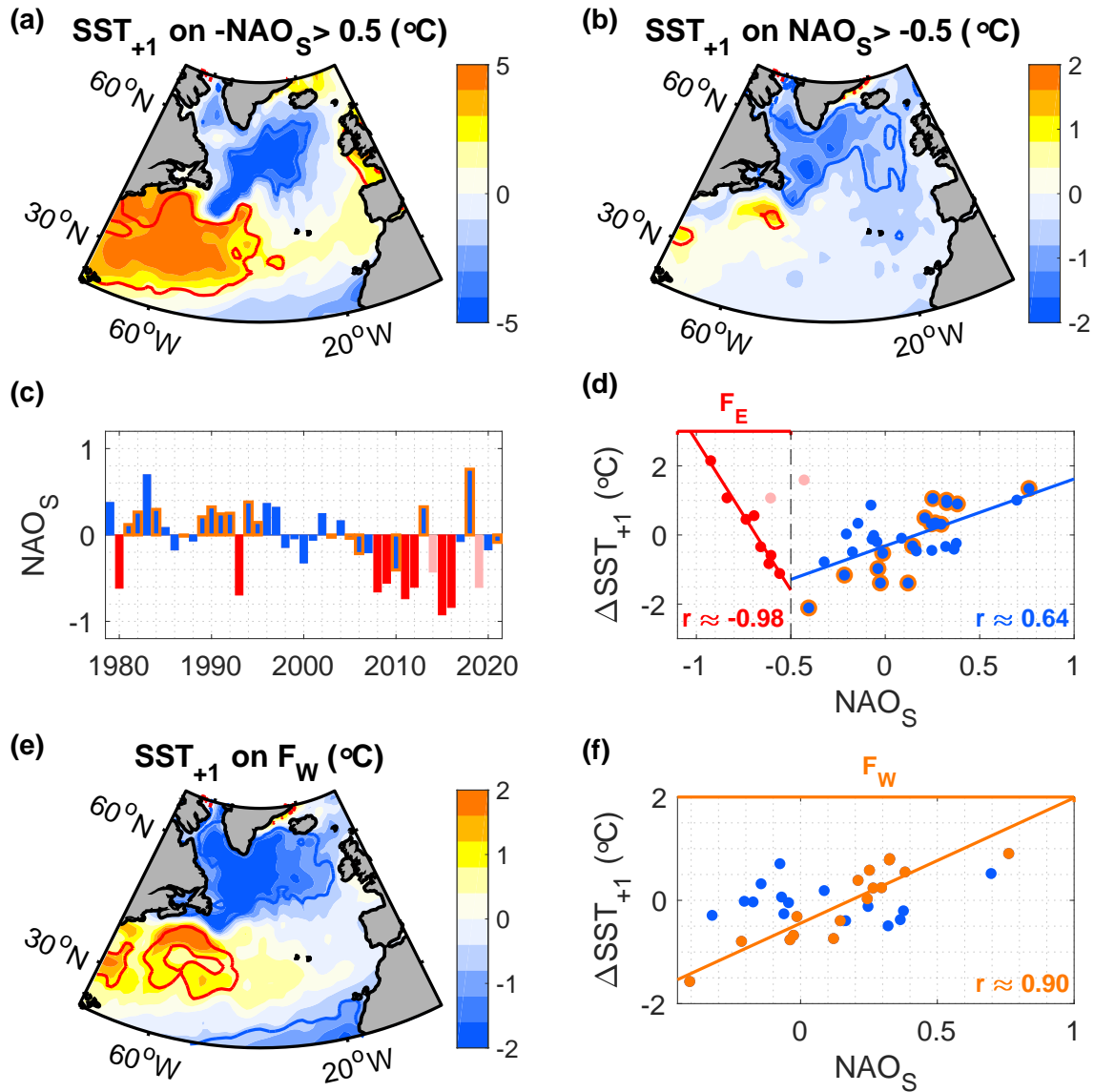
Figure A1. (a,b) Regression of the SST in winter (January through to March) on (a) $-NAO_S$ from the preceding summer for the years in which $-NAO_S > 0.5$, and (b) $+NAO_S$ from the preceding summer for the years in which $+NAO_S > -0.5$, excluding the two outliers. Contours encompass regions that are significant at the 95% confidence level. (c) Variability of the mean NAO index in July and August (NAO_S), with the colour coding matching that in d. (d) Relationship between NAO_S and the subsequent winter SST, where ΔSST corresponds to the SST difference between the red and blue 95% confidence regions in a (red years) and b (blue years) respectively, relative to the climatological mean. (e,f) Regression of the SST in winter on the subsampled NAO_S from the preceding summer (colour coded in orange in c, d and f), where ΔSST in f corresponds to the SST difference between the red and blue 95% confidence regions in e.

A3 Evaluating the surface mass balance

Taking advantage of the newly derived, strong relationships between the NAO_S subsets and subsequent SST anomalies, we next regress each term in Eq. (A2) on the optimised NAO_S subsets and evaluate the surface mass balance over the cold anomaly regions within the regions enclosed by the 95% confidence lines (Figs. A2a and A3a).

First, we estimate the horizontal transports A. On the timescales and spatial scales considered, the strongest horizontal velocities result from geostrophic flows, which do not contribute to the mass balance as they are along density contours. Therefore, we only consider ageostrophic transports. The largest ageostrophic flows in the open ocean result from the wind forcing, which we evaluate using the wind stresses from the atmospheric reanalysis ERA5. Integrated over the winter period (January through to March), we find that neither the horizontal Ekman transports nor the vertical Ekman pumping can account for the density increase associated with the cold anomaly. They are not significantly correlated with the freshwater indices, their amplitudes are too small, and their directions are inconsistent with the cold anomaly (Figs. A2a, b and A3a, b).

Next, we estimate the buoyancy flux anomalies $B = \frac{g\alpha}{c_p}Q + g\beta S (P - E)$, where c_p is the heat capacity, Q is the heat flux (positive downward) and $P - E$ is the freshwater flux in kg m^{-2} s^{-1} (Gill, 2016). After evaluating the buoyancy fluxes with the ERA5 6-hourly surface heat and freshwater fluxes and regressing them on the freshwater indices, we find that they do not match the distribution of the SST (Figs. A2c and A3c). The surface heat fluxes, which have the largest contribution to the buoyancy fluxes, are also not significantly correlated with the freshwater indices (Figs. A2d and A3d).

To estimate the influence of the buoyancy fluxes on the density, we use mean mixed layer depths of 250 m and 280 m in the cold anomaly regions associated with F_E and F_W respectively, obtained from Argo float profiles (Holte et al., 2017). When averaged over the cold anomaly and integrated over the winter, the buoyancy flux anomaly after melt-induced freshwater events reflects an anomalous mass decrease of $\sim$7 kg m^{-2} whereas the cold anomaly implies a mass increase of $\sim$204 kg m^{-2}. After circulation-induced freshwater events, the buoyancy flux anomaly reflects an anomalous mass decrease of $\sim$5 kg m^{-2}, whereas the cold anomaly implies a mass increase of $\sim$74 kg m^{-2}.

The anomalous mass flux through the mixed layer base must have the same sign as the mass flux through the surface and the mixed layer depth anomaly, regardless of whether the surface flux anomaly is driven by preexisting density anomalies in the ocean ("M drives B") or the atmosphere ("B drives M"). With the buoyancy fluxes, vertical Ekman transports and horizontal advection being negligible, there cannot be an anomalous density flux through the base of the mixed layer. The mixed layer can only entrain water of the same density as that at the surface. If anomalously cold water from below is entrained, it must also be anomalously fresh.

Since for both F_W and F_E, the surface buoyancy flux anomalies are positive, the ocean loses less heat (M drives B), and the mixed layer is slightly shallower and lighter when averaged over the investigated regions. As shown above, however, the density changes implied by the surface fluxes associated with both F_W and F_E are over one order of magnitude smaller than the density changes implied by the cold anomalies. Thus, the change in the mixed layer depth and any overcompensation of the density anomaly — by a surplus of surface freshening, a slowdown of the buoyancy-driven overturning circulation, preexisting density anomalies, or any other buoyancy-driven mechanism — is negligible on the timescales considered.
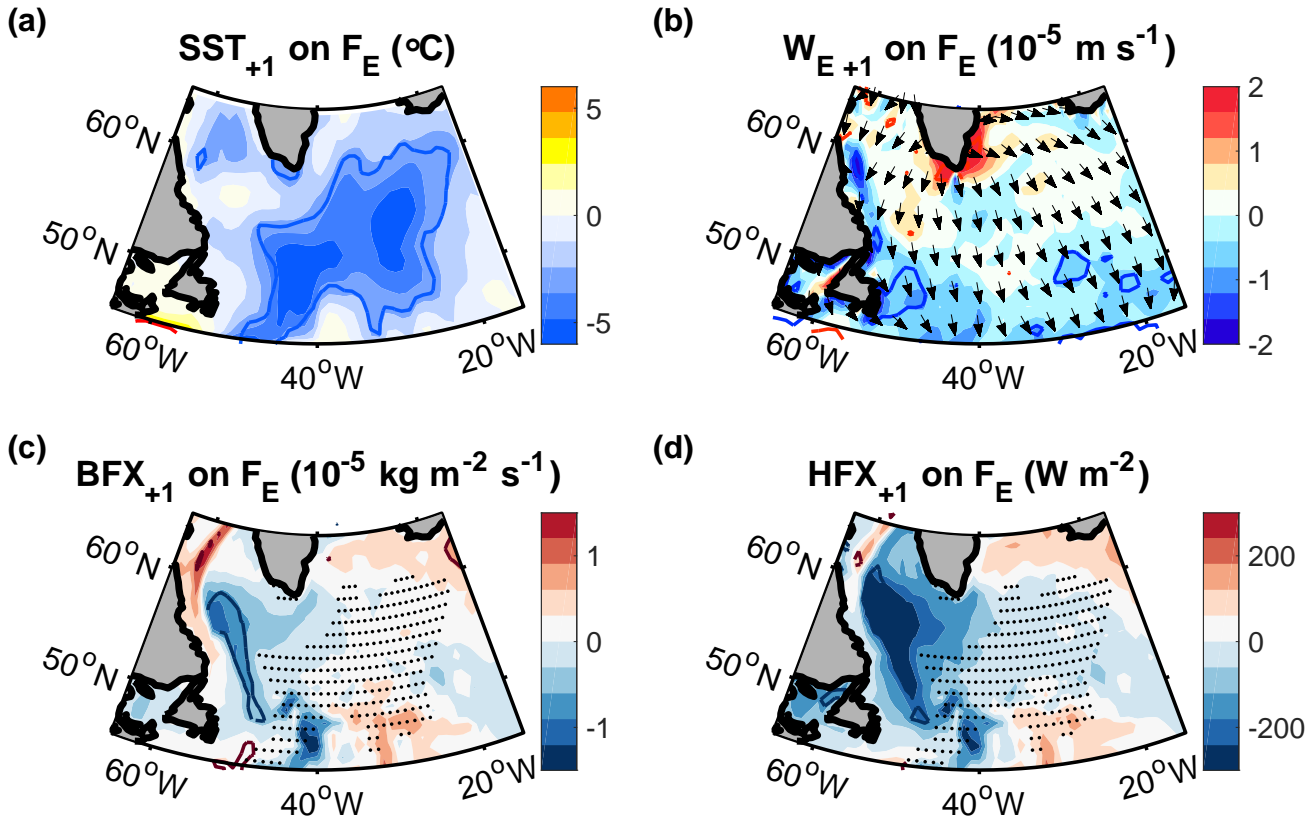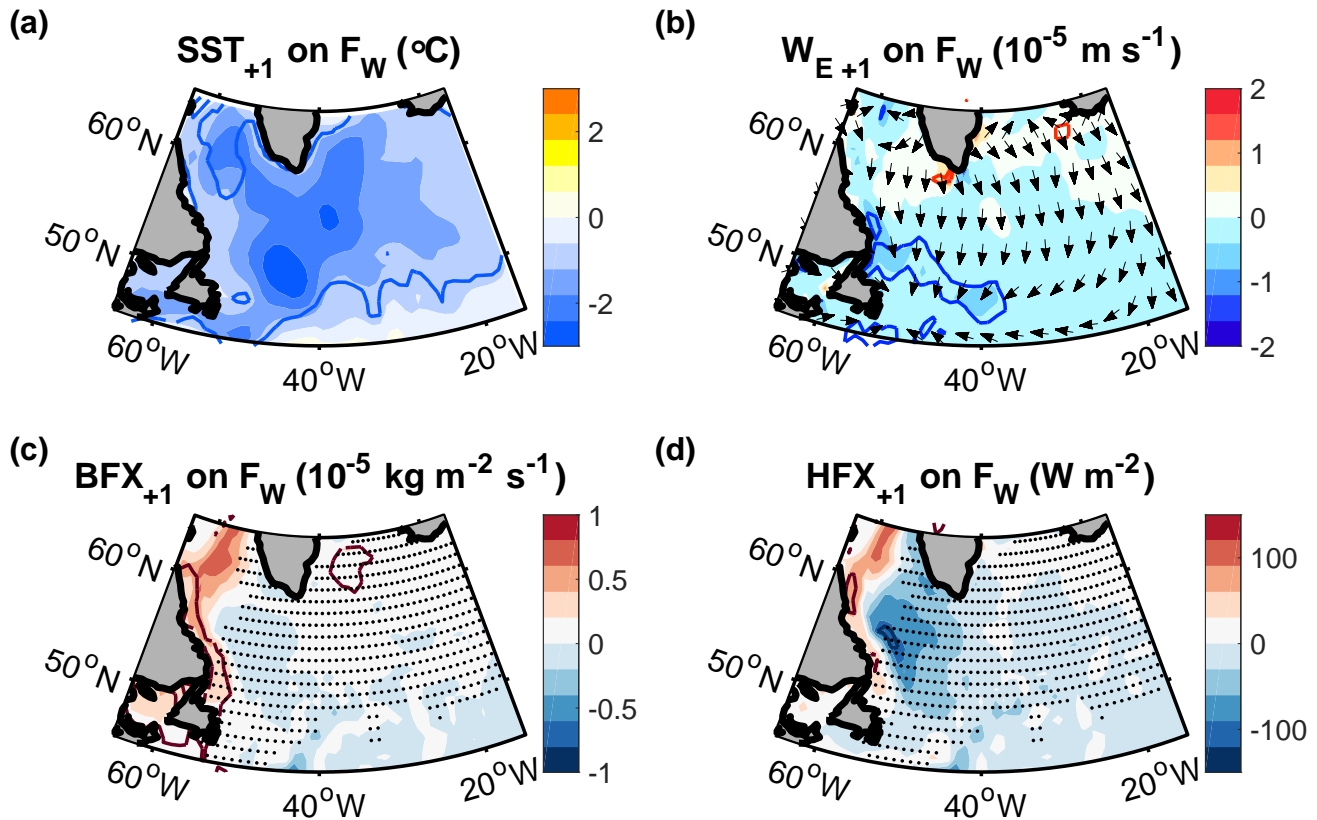
Figure A2. Regression of (a) the SST, (b) the vertical Ekman velocity (positive upward), (c) the buoyancy flux anomaly (positive downward) and (d) the surface heat fluxes (also positive downward) in winter (January through March) on F_E from the preceding summer. The arrows in (b) indicate the direction of the horizontal Ekman transports and the dots in (c) and (d) show the region used for the mass balance calculations, corresponding to the cold anomaly region. Contours encompass regions that are significant at the 95% confidence level.

A4 Outcome

Since none of the potential drivers of density anomalies on the righthand side of Eq. (A1) can account for the the density increase associated with the cold anomaly, we conclude that the density increase associated with the cold anomaly must be balanced by a density decrease associated with a freshwater anomaly $\alpha \partial T_E \approx \beta \partial S_E$, and similarly for the F_W subset. The buoyancy fluxes represent the largest term on the righthand side of Eq. (A2) and thus determine the uncertainty of the obtained salinity estimates, amounting to 4% for the F_E subset and 7% for the F_W subset.

While the SST does not need to be equal to the mixed layer temperature, the constant density profile in the mixed layer implies that any temperature change within the mixed layer must be accompanied by a salinity change that compensates for the density change. Thus, the relationship between the SST and the sea surface salinity (SSS) is the same as that between the mixed layer temperature and salinity, both for F_E: $\alpha \partial (SST_E) \approx \beta \partial (SSS_E)$, and F_W: $\alpha \partial (SST_W) \approx \beta \partial (SSS_W)$.

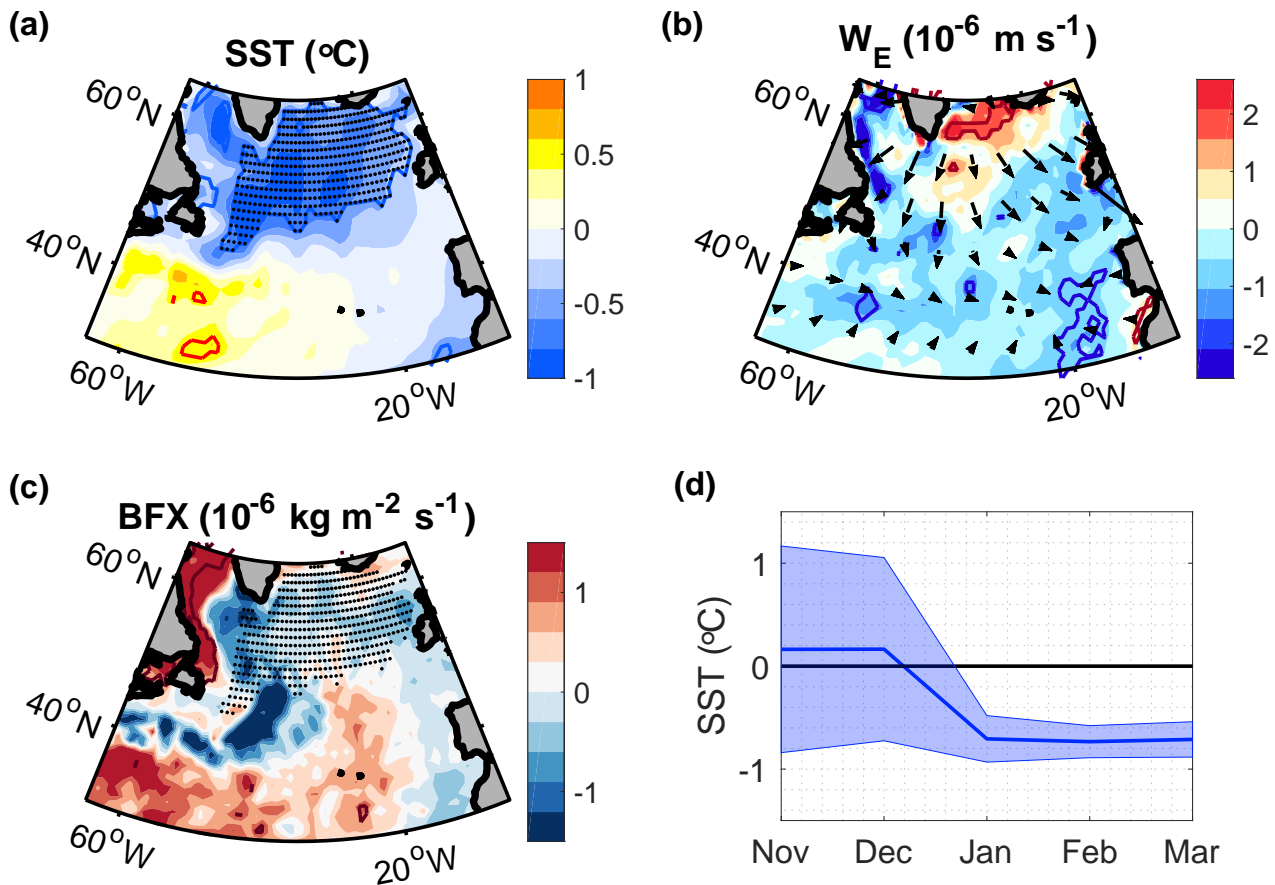**Figure A3.** Regression of (a) the SST, (b) the vertical Ekman velocity (positive upward), (c) the buoyancy flux anomaly (positive downward) and (d) the surface heat fluxes (also positive downward) in winter (January through March) on F_W from the preceding summer. The arrows in (b) indicate the direction of the horizontal Ekman transports and the dots in (c) and (d) show the region used for the mass balance calculations. Contours encompass regions that are significant at the 95% confidence level.

445   To verify the robustness of the results, we tested different integration periods and regions for the mass balance calculations. For instance, we also integrated the transports and surface fluxes from September to March instead of January to March, and we extended the investigated region over the full cold anomaly region, over which the SST anomaly is negative. In each case, the results did not change appreciably.

    The mass balance analyses demonstrate that both indices allow us to estimate the variability of freshwater from the SST
450 with high accuracies. Physically, the identified density compensation of the temperature and salinity anomalies implies that the freshwater anomaly determines the temperature that the surface water is required to have before it can be mixed down.

A5   Surface mass balance for composite analysis

Next, we analysed the surface mass balance for the composites of the cold anomaly in the winters preceding the 10 warmest relative to the 10 coldest summers over Europe (Fig. 10). We obtained qualitatively similar patterns compared to those asso-
455   ciated with the two freshwater indices. Again, we find that none of the density drivers on the righthand side of Eq. (A2) show a significant signal over the cold anomaly region, and their amplitudes cannot account for the density increase implied by the cold anomaly (Fig. A4). The surface buoyancy flux, which is the largest term on the righthand side of Eq. (A2), amounts to $\sim+1.3$ g kg^{-1} while density anomaly implied by the cold anomaly is ~-40 g kg^{-1}. Thus, the uncertainty of the estimated freshwater anomaly (Fig. 10e) is ~3 %.

Figure A4. (a,b,c) Anomaly of (a) the SST, (b) the vertical Ekman velocity (positive upward) and (c) the buoyancy flux anomaly (positive downward) in the winters (January through March) before the summers of the heat wave composites (Fig. 10). The arrows in (b) indicate the direction of the horizontal Ekman transports and the dots in (a) and (c) mark the region of the mass balance calculations. (d) Evolution of the SST anomaly during these winters in the cold anomaly region. The shading represents the standard error.

460   A6   Testing the freshwater indices with hydrographic observations

To confirm that the two derived freshwater indices, F_E and F_W, are associated with freshwater anomalies, we use in-situ hydrographic observations from the Labrador Sea convection region, identified and selected based on closed absolute dynamic topography contours (Fig. A5). Using observations from the Labrador Sea convection region has the advantage that the spatial variability is smallest, allowing us to construct meaningful, continuous time series of the hydrographic variability in the

465   Labrador Sea from 2002 to 2022, when sufficient Argo float observations are available (Oltmanns et al., 2020).
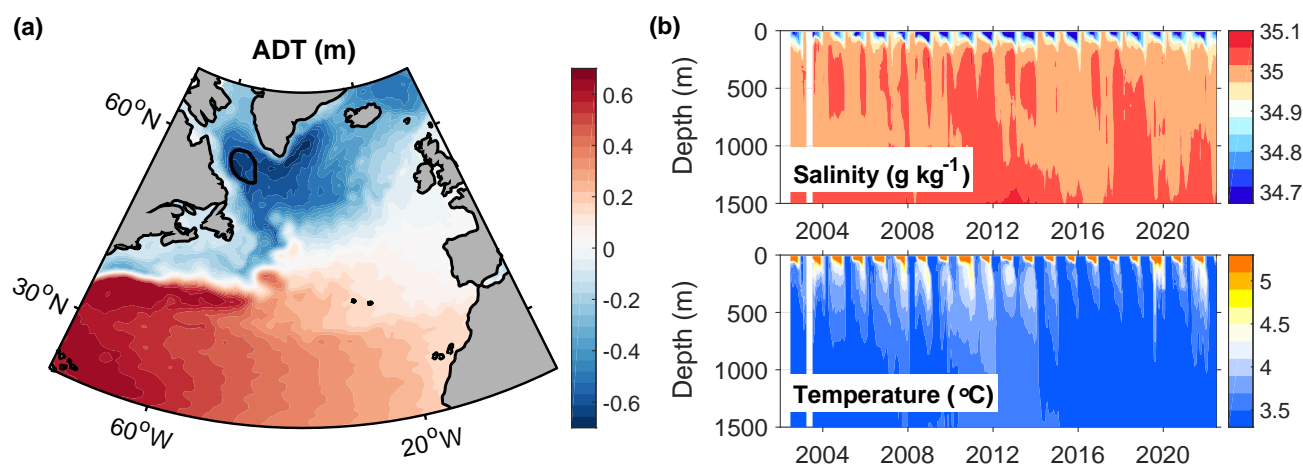
Figure A5. (a) Mean absolute dynamic topography with the region, used for the Argo float sampling, indicated by the black contour. (b) Time series of the absolute salinity and potential temperature from Argo floats, constructed by averaging the obtained Argo float profiles within the sampling region over two-week intervals (Oltmanns et al., 2020).

While the Labrador Sea has the advantage of small spatial variability, it also has the disadvantage that it is characterised by the largest surface heat fluxes (Fig. A2d and A3d), mixing surface freshwater down. Thus, there are no significant surface freshwater anomalies in the Labrador Sea convection centre associated with the indices (Fig. 3). Still, it is possible to trace the freshwater anomalies below the surface, after they have been mixed down.

470   To investigate the link between the freshwater indices and the subsurface hydrography in the Labrador Sea, we regress the hydrographic time series onto the two freshwater indices. Given the comparatively short time period of the hydrographic observations, we do not further apply any subsampling to the indices after removing the two outliers (Fig. A1d), resulting in 6 available years for the F_E subset and in 13 available years for the F_W subset.

As predicted by the mass balance analysis, we identify significant cold and fresh anomalies linked to both indices. The F_W

475   subset is associated with deeper and relatively weaker fresh and cold anomalies, that already enter the sampling region during autumn (Fig. A6a and c). For the F_E subset, the fresh and cold anomalies are shallower and stronger (Fig. A6b and d), and they reach their maximum amplitude during winter.
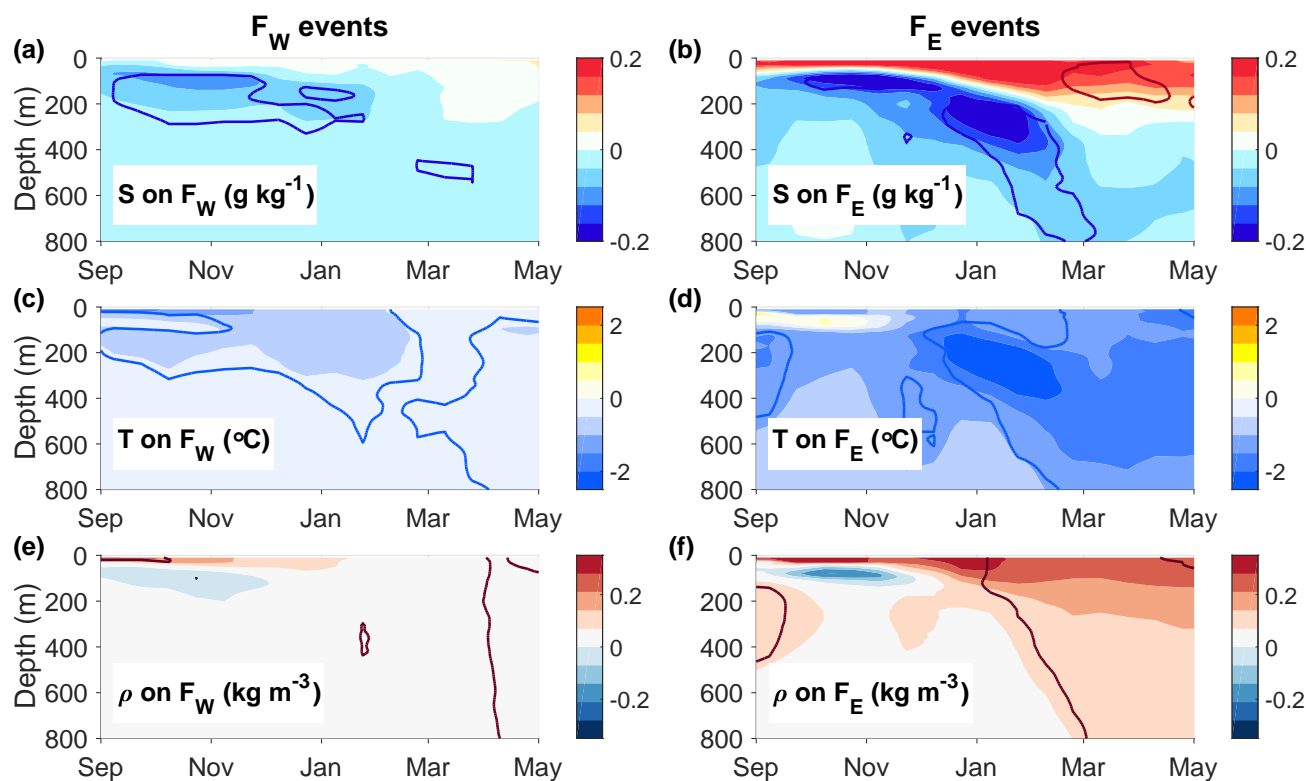
Figure A6. Regressions of the absolute salinity, potential temperature and density onto the freshwater indices F_W and F_E, based on the hydrographic time series shown in Figure A5b.

In addition, we find that the F_E subset is associated with a significant densification of the water column, implying that the temperature and salinity anomalies do not exactly compensate for each other (Fig. A6e and f). However, we show based on the freshwater anomalies in the winters 2015 and 2016, that even under particularly intense surface heat fluxes, and even in the Labrador Sea, where the largest densification occurs, the surface mass balance still provides a good approximation of the salinity anomalies, with root mean square errors below $\sim$0.09 g kg^{-1} (Appendix A7). This important finding implies that even under particularly intense surface fluxes, and even in the Labrador Sea, the additional temperature change achieved by the surface fluxes is still much smaller than the temperature anomalies implied by the freshwater anomalies.

We conclude that, despite the limitations of the hydrographic dataset and the limited number of available years, the freshwater anomalies are reproduced for both indices. Still, we point out that the method of inferring freshwater anomalies from the surface mass balance provides superior freshwater estimates because it has a better spatial and temporal coverage, with longer time spans and higher spatial and temporal resolution.

A7 Example of surface mass balance in hydrographic observations

490 Next, we use hydrographic observations from Argo floats for the full subpolar region. We focus on the extreme winters 2015 and 2016, characterised by particularly large surface fluxes and deep convection (Yashayaev and Loder, 2017; Piron et al., 2017). In both winters, we find that temperature and salinity anomalies are well-correlated with each other ($r \approx 0.72$, $p \approx 5 \cdot 10^{-242}$, based on 1532 profiles). Moreover, the observed salinity anomalies are well-aligned with the estimated salinity anomalies, obtained by assuming density compensation (Fig. A7). The root mean square error resulting from using a mass balance amounts to

495 ~ 0.09 g kg^{-1}, smaller than that of currently available salinity products (Bao et al., 2019; Xie et al., 2019). Thus, even in this case of intense surface fluxes, the surface mass balance still provides a good approximation of the freshwater anomalies.
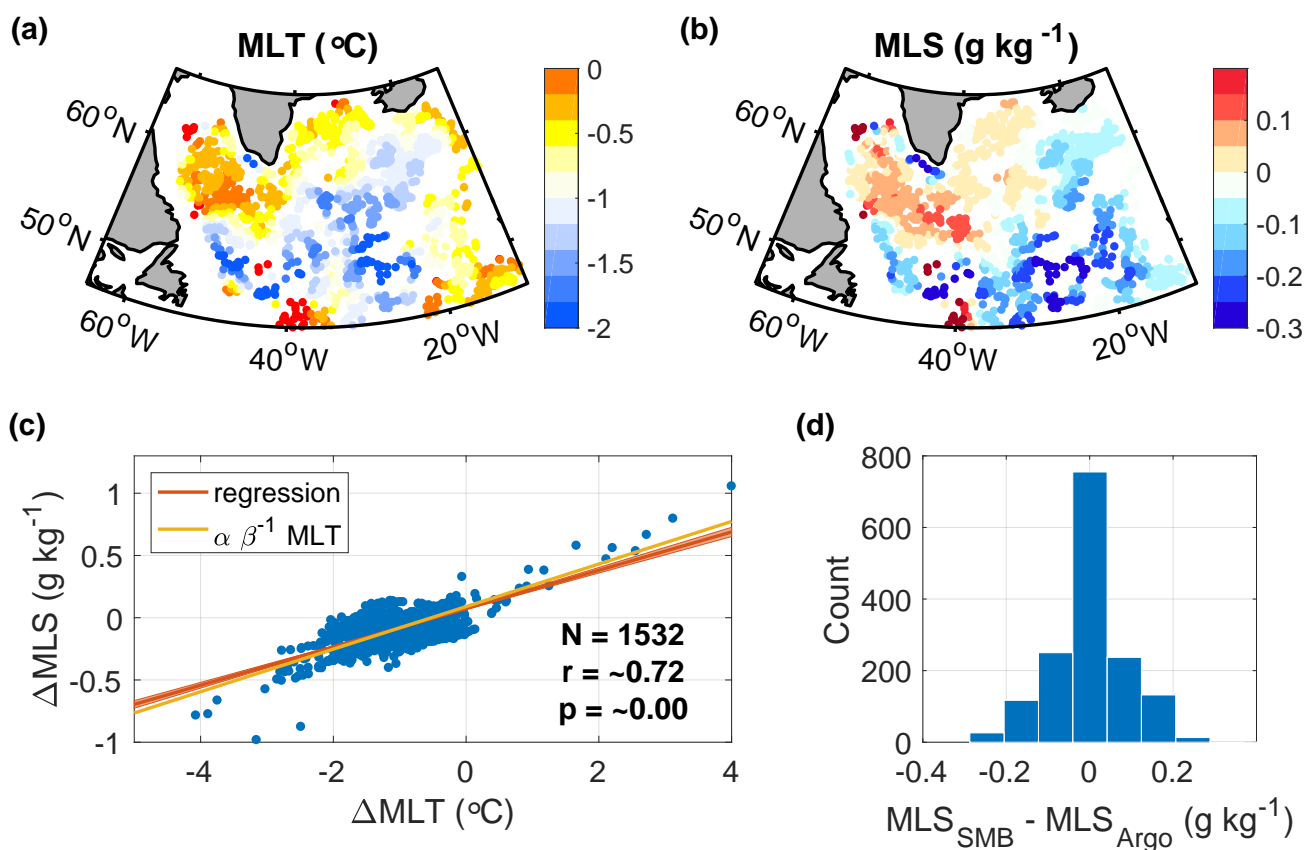

Figure A7. (a,b) Mixed layer temperature (MLT) and salinity (MLS) anomalies in the winters of 2015 and 2016 (January to April), derived from Argo profiles (Holte et al., 2017). The anomalies are relative to the climatological mean, estimated by averaging all other wintertime profiles within 2° longitude and 1° latitude. (c) Linear regression of the observed MLS anomalies on the MLT anomalies (red line), and the MLS estimate obtained by assuming density compensation (yellow line). (d) Differences between the estimated and observed MLS anomalies. The associated root mean square error is ~ 0.09 g kg^{-1}.

Appendix B: Simulated atmospheric response to the freshwater-induced SST in winter

To support the role of the SST pattern in driving the observed atmospheric response in winters after freshwater events (Fig. 4b), we define an SST index that captures the time variability of the spatial SST pattern linked to freshwater events. Specifically,

500 we project the SST each winter onto the observed SST pattern after freshwater events (Fig. B1a and b). The projection is obtained from a linear least-square fit of the SST each winter to the observed pattern after freshwater events. We then regress the atmospheric streamfunction at different pressure levels onto this SST index, using 50 ensemble simulations from ECHAM5, performed with prescribed observation-based SSTs.

The SST-forced model simulations support that the SST pattern associated with freshwater events leads to a significant

505 atmospheric circulation anomaly over the North Atlantic, extending deep into the troposphere (Fig. B1c and d). As in the observations, the simulated fields are characterised by a cyclonic circulation anomaly in the subpolar region and an anticyclonic circulation anomaly in the subtropical region. The winds at 250 hPa are still following the underlying SST gradients. Since the simulations were SST-forced, they imply that the obtained atmospheric circulation pattern is driven by the SST, although the SST is itself also the result of atmospheric feedbacks. While a detailed description of the involved diagnostics is beyond

510 the scope of this study, the obtained atmospheric response is consistent with theoretical expectations (Eady, 1949), and the underlying dynamics are well-understood (O'Reilly et al., 2017; Omrani et al., 2019).

We point out that the SST_{FW} pattern (Fig. B1a and b) is specific to the North Atlantic. It was obtained using a projection of the SST each winter onto the SST after freshwater events (Fig. 2a), north of 30 °N. The results are not sensitive to the selected region as long as it includes the enhanced SST front between the subtropical and subpolar gyre. We do not find any significant

515 links of the obtained SST_{FW} pattern to the El Niño Southern Oscillation in the Pacific or to the SST in the South Atlantic.
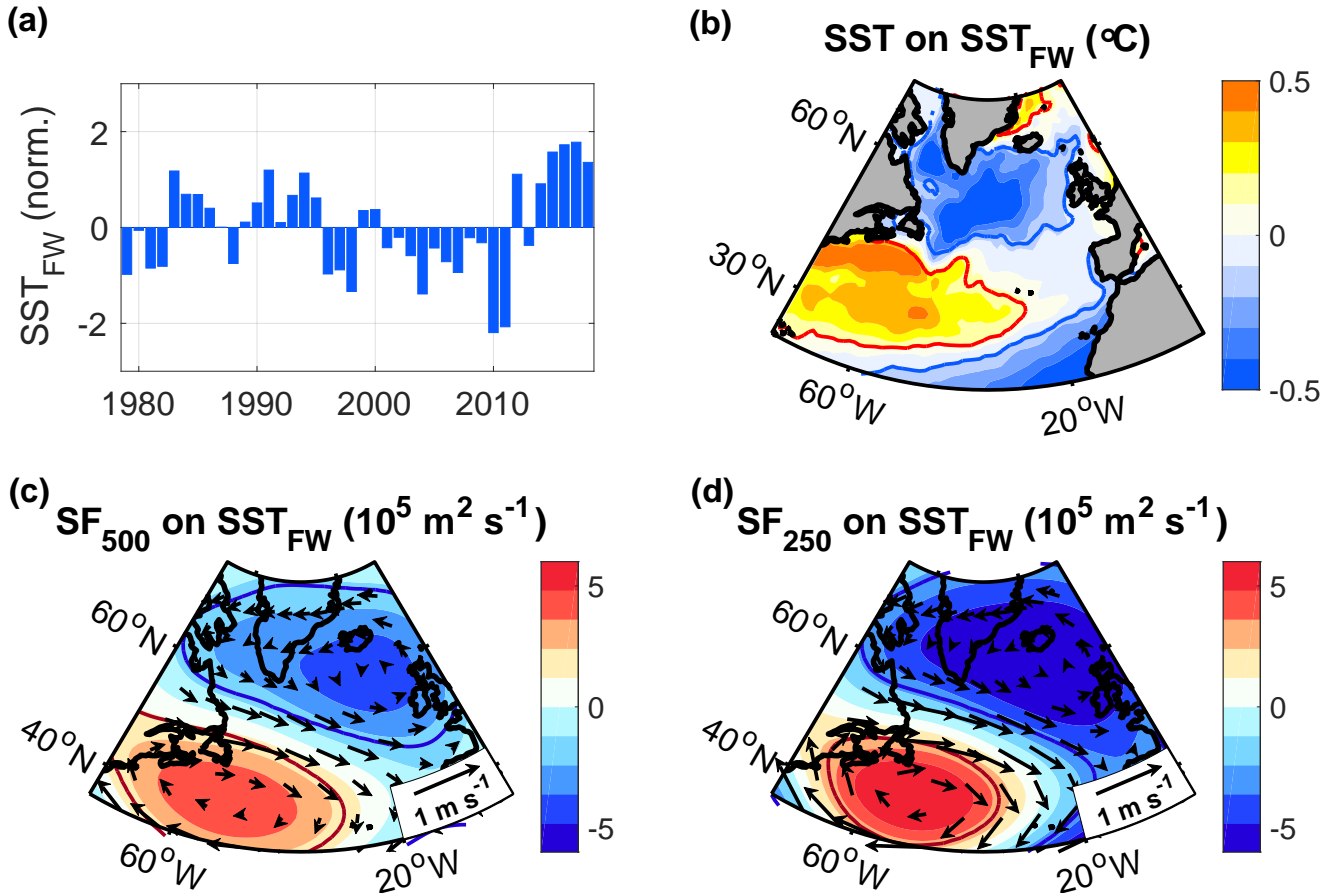
Figure B1. (a) Variability and (b) distribution of the freshwater-induced SST pattern in winter (January through March), obtained by projecting the SST each winter on the North Atlantic SST (north of 30 °N) after freshwater events (Fig. 2a). Thus, SST_{FW} represents the temporal variability of the spatial SST pattern linked to freshwater events. (c,d) Regressions of the simulated stream function and winds in winter at (c) 500 hPa and (d) 250 hPa onto the normalised SST_{FW} pattern shown in (a) and (b). The simulations were acquired from 50 ensemble members from ECHAM5, performed with prescribed observation-based SST over the period 1979–2018. Contours encompass regions that are significant at the 95% confidence level.

References

Arribas, A., Glover, M., Maidens, A., Peterson, K., Gordon, M., MacLachlan, C., Graham, R., Fereday, D., Camp, J., Scaife, A., et al.: The GloSea4 ensemble prediction system for seasonal forecasting, Monthly Weather Review, 139, 1891–1910, 2011.

Bamber, J., Tedstone, A., King, M., Howat, I., Enderlin, E., van den Broeke, M., and Noel, B.: Land ice freshwater budget of the Arctic and North Atlantic Oceans: 1. Data, methods, and results, Journal of Geophysical Research: Oceans, 123, 1827–1837, 2018.

Bao, S., Wang, H., Zhang, R., Yan, H., and Chen, J.: Comparison of satellite-derived sea surface salinity products from SMOS, Aquarius, and SMAP, Journal of Geophysical Research: Oceans, 124, 1932–1944, 2019.

Barnes, E. A.: Revisiting the evidence linking Arctic amplification to extreme weather in midlatitudes, Geophysical research letters, 40, 4734–4739, 2013.

Barnston, A. G. and Livezey, R. E.: Classification, seasonality and persistence of low-frequency atmospheric circulation patterns, Monthly weather review, 115, 1083–1126, 1987.

Blackport, R. and Screen, J. A.: Insignificant effect of Arctic amplification on the amplitude of midlatitude atmospheric waves, Science advances, 6, eaay2880, 2020.

Böning, C. W., Behrens, E., Biastoch, A., Getzlaff, K., and Bamber, J. L.: Emerging impact of Greenland meltwater on deepwater formation in the North Atlantic Ocean, Nature Geoscience, 9, 523–527, 2016.

Briner, J. P., Cuzzone, J. K., Badgeley, J. A., Young, N. E., Steig, E. J., Morlighem, M., Schlegel, N.-J., Hakim, G. J., Schaefer, J. M., Johnson, J. V., et al.: Rate of mass loss from the Greenland Ice Sheet will exceed Holocene values this century, Nature, 586, 70–74, 2020.

Carmack, E. C., Yamamoto-Kawai, M., Haine, T. W., Bacon, S., Bluhm, B. A., Lique, C., Melling, H., Polyakov, I. V., Straneo, F., Timmermans, M.-L., et al.: Freshwater and its role in the Arctic Marine System: Sources, disposition, storage, export, and physical and biogeochemical consequences in the Arctic and global oceans, Journal of Geophysical Research: Biogeosciences, 121, 675–717, 2016.

Cohen, J., Screen, J. A., Furtado, J. C., Barlow, M., Whittleston, D., Coumou, D., Francis, J., Dethloff, K., Entekhabi, D., Overland, J., et al.: Recent Arctic amplification and extreme mid-latitude weather, Nature geoscience, 7, 627–637, 2014.

Cohen, J., Zhang, X., Francis, J., Jung, T., Kwok, R., Overland, J., Ballinger, T., Bhatt, U., Chen, H., Coumou, D., et al.: Divergent consensuses on Arctic amplification influence on midlatitude severe winter weather, Nature Climate Change, pp. 1–10, 2019.

Czaja, A. and Frankignoul, C.: Observed impact of Atlantic SST anomalies on the North Atlantic Oscillation, Journal of Climate, 15, 606–623, 2002.

Davies, H. and Bishop, C.: Eady edge waves and rapid development, Journal of the atmospheric sciences, 51, 1930–1946, 1994.

Dierer, S., Schluenzen, K. H., et al.: Influence parameters for a polar mesocyclone development, METEOROLOGISCHE ZEITSCHRIFT-BERLIN-, 14, 781, 2005.

Dong, B., Sutton, R. T., Woollings, T., and Hodges, K.: Variability of the North Atlantic summer storm track: Mechanisms and impacts on European climate, Environmental Research Letters, 8, 034 037, 2013.

Duchez, A., Frajka-Williams, E., Josey, S. A., Evans, D. G., Grist, J. P., Marsh, R., McCarthy, G. D., Sinha, B., Berry, D. I., and Hirschi, J. J.: Drivers of exceptionally cold North Atlantic Ocean temperatures and their link to the 2015 European heat wave, Environmental Research Letters, 11, 074 004, 2016.

Dukhovskoy, D., Yashayaev, I., Proshutinsky, A., Bamber, J., Bashmachnikov, I., Chassignet, E., Lee, C., and Tedstone, A.: Role of Greenland freshwater anomaly in the recent freshening of the subpolar North Atlantic, Journal of Geophysical Research: Oceans, 124, 3333–3360, 2019.

Dunstone, N., Smith, D., Scaife, A., Hermanson, L., Fereday, D., O'Reilly, C., Stirling, A., Eade, R., Gordon, M., MacLachlan, C., et al.: Skilful seasonal predictions of summer European rainfall, Geophysical Research Letters, 45, 3246–3254, 2018.

Eady, E. T.: Long waves and cyclone waves, Tellus, 1, 33–52, 1949.

565 Francis, J. A. and Vavrus, S. J.: Evidence linking Arctic amplification to extreme weather in mid-latitudes, Geophysical research letters, 39, 2012.

Gervais, M., Shaman, J., and Kushnir, Y.: Impact of the North Atlantic Warming Hole on Sensible Weather, Journal of Climate, 33, 4255–4271, 2020.

Gill, A. E.: Atmosphere—ocean dynamics, Elsevier, 2016.

570 Häkkinen, S. and Rhines, P. B.: Shifting surface currents in the northern North Atlantic Ocean, Journal of Geophysical Research: Oceans, 114, 2009.

Häkkinen, S., Rhines, P. B., and Worthen, D. L.: Warm and saline events embedded in the meridional circulation of the northern North Atlantic, Journal of Geophysical Research: Oceans, 116, 2011.

Häkkinen, S., Rhines, P. B., and Worthen, D. L.: Northern North Atlantic sea surface height and ocean heat content variability, Journal of
575 Geophysical Research: Oceans, 118, 3670–3678, 2013.

Hanna, E., Jones, J. M., Cappelen, J., Mernild, S. H., Wood, L., Steffen, K., and Huybrechts, P.: The influence of North Atlantic atmospheric and oceanic forcing effects on 1900–2010 Greenland summer climate and ice melt/runoff, International Journal of Climatology, 33, 862–880, 2013.

Hanna, E., Cappelen, J., Fettweis, X., Mernild, S. H., Mote, T. L., Mottram, R., Steffen, K., Ballinger, T. J., and Hall, R. J.: Greenland
580 surface air temperature changes from 1981 to 2019 and implications for ice-sheet melt and mass-balance change, International Journal of Climatology, 41, E1336–E1352, 2021.

Hersbach, H., Bell, B., Berrisford, P., Biavati, G., Horányi, A., Muñoz Sabater, J., Nicolas, J., Peubey, C., Radu, R., Rozum, I., et al.: ERA5 hourly data on single levels from 1979 to present, Copernicus Climate Change Service (C3S) Climate Data Store (CDS), 10, 2018.

Heuzé, C.: North Atlantic deep water formation and AMOC in CMIP5 models, Ocean Science, 13, 609, 2017.

585 Holliday, N. P., Bersch, M., Berx, B., Chafik, L., Cunningham, S., Florindo-López, C., Hátún, H., Johns, W., Josey, S. A., Larsen, K. M. H., et al.: Ocean circulation causes the largest freshening event for 120 years in eastern subpolar North Atlantic, Nature Communications, 11, 1–15, 2020.

Holte, J., Talley, L. D., Gilson, J., and Roemmich, D.: An Argo mixed layer climatology and database, Geophysical Research Letters, 44, 5618–5626, 2017.

590 Hurrell, J. W., Hack, J. J., Shea, D., Caron, J. M., and Rosinski, J.: A new sea surface temperature and sea ice boundary dataset for the Community Atmosphere Model, Journal of Climate, 21, 5145–5153, 2008.

Khan, S. A., Aschwanden, A., Bjørk, A. A., Wahr, J., Kjeldsen, K. K., and Kjaer, K. H.: Greenland ice sheet mass balance: a review, Reports on progress in physics, 78, 046 801, 2015.

Kostov, Y., Johnson, H. L., Marshall, D. P., Heimbach, P., Forget, G., Holliday, N. P., Lozier, M. S., Li, F., Pillar, H. R., and Smith, T.: Distinct
595 sources of interannual subtropical and subpolar Atlantic overturning variability, Nature Geoscience, 14, 491–495, 2021.

Kumar, A., Yadav, J., and Mohan, R.: Global warming leading to alarming recession of the Arctic sea-ice cover: Insights from remote sensing observations and model reanalysis, Heliyon, 6, e04 355, 2020.

Le Traon, P., Nadal, F., and Ducet, N.: An improved mapping method of multisatellite altimeter data, Journal of atmospheric and oceanic technology, 15, 522–534, 1998.

600 Lindzen, R. and Farrell, B.: A simple approximate result for the maximum growth rate of baroclinic instabilities, Journal of the atmospheric sciences, 37, 1648–1654, 1980.

Liu, W., Xie, S.-P., Liu, Z., and Zhu, J.: Overlooked possibility of a collapsed Atlantic Meridional Overturning Circulation in warming climate, Science Advances, 3, e1601 666, 2017.

Marshall, J., Johnson, H., and Goodman, J.: A study of the interaction of the North Atlantic Oscillation with ocean circulation, Journal of
605 Climate, 14, 1399–1421, 2001.

Marzocchi, A., Hirschi, J. J.-M., Holliday, N. P., Cunningham, S. A., Blaker, A. T., and Coward, A. C.: The North Atlantic subpolar circulation in an eddy-resolving global ocean model, Journal of Marine Systems, 142, 126–143, 2015.

Mecking, J., Drijfhout, S., Jackson, L., and Andrews, M.: The effect of model bias on Atlantic freshwater transport and implications for AMOC bi-stability, Tellus A: Dynamic Meteorology and Oceanography, 69, 1299 910, 2017.

610 Mecking, J., Drijfhout, S., Hirschi, J. J., and Blaker, A.: Ocean and atmosphere influence on the 2015 European heatwave, Environmental Research Letters, 14, 114 035, 2019.

Menary, M. B., Hodson, D. L., Robson, J. I., Sutton, R. T., Wood, R. A., and Hunt, J. A.: Exploring the impact of CMIP5 model biases on the simulation of North Atlantic decadal variability, Geophysical Research Letters, 42, 5926–5934, 2015.

Müller, V., Kieke, D., Myers, P. G., Pennelly, C., Steinfeldt, R., and Stendardo, I.: Heat and freshwater transport by mesoscale eddies in the
615 southern subpolar North Atlantic, Journal of Geophysical Research: Oceans, 124, 5565–5585, 2019.

Munk, W. H.: On the wind-driven ocean circulation, Journal of Atmospheric Sciences, 7, 80–93, 1950.

Murray, D., Hoell, A., Hoerling, M., Perlwitz, J., Quan, X.-W., Allured, D., Zhang, T., Eischeid, J., Smith, C. A., Barsugli, J., et al.: Facility for Weather and Climate Assessments (FACTS): A Community Resource for Assessing Weather and Climate Variability, Bulletin of the American Meteorological Society, 101, E1214–E1224, 2020.

620 Neale, R. B., Chen, C.-C., Gettelman, A., Lauritzen, P. H., Park, S., Williamson, D. L., Conley, A. J., Garcia, R., Kinnison, D., Lamarque, J.-F., et al.: Description of the NCAR community atmosphere model (CAM 5.0), NCAR Tech. Note NCAR/TN-486+ STR, 1, 1–12, 2012.

Notz, D. and Stroeve, J.: The trajectory towards a seasonally ice-free Arctic ocean, Current climate change reports, 4, 407–416, 2018.

Oltmanns, M., Karstensen, J., Moore, G., and Josey, S. A.: Rapid cooling and increased storminess triggered by freshwater in the North Atlantic, Geophysical Research Letters, p. e2020GL087207, 2020.

625 Omrani, N.-E., Ogawa, F., Nakamura, H., Keenlyside, N., Lubis, S. W., and Matthes, K.: Key Role of the Ocean Western Boundary currents in shaping the Northern Hemisphere climate, Scientific reports, 9, 1–12, 2019.

O'Reilly, C. H., Minobe, S., Kuwano-Yoshida, A., and Woollings, T.: The Gulf Stream influence on wintertime North Atlantic jet variability, Quarterly Journal of the Royal Meteorological Society, 143, 173–183, 2017.

Osborne, J. M., Collins, M., Screen, J. A., Thomson, S. I., and Dunstone, N.: The North Atlantic as a driver of summer atmospheric
630 circulation, Journal of Climate, 33, 7335–7351, 2020.

Overland, J., Francis, J. A., Hall, R., Hanna, E., Kim, S.-J., and Vihma, T.: The melting Arctic and midlatitude weather patterns: Are they connected?, Journal of Climate, 28, 7917–7932, 2015.

Piron, A., Thierry, V., Mercier, H., and Caniaux, G.: Gyre-scale deep convection in the subpolar North Atlantic Ocean during winter 2014–2015, Geophysical Research Letters, 44, 1439–1447, 2017.

635 Rayner, N., Parker, D. E., Horton, E., Folland, C. K., Alexander, L. V., Rowell, D., Kent, E., and Kaplan, A.: Global analyses of sea surface temperature, sea ice, and night marine air temperature since the late nineteenth century, Journal of Geophysical Research: Atmospheres, 108, 2003.

Reynolds, R. W., Rayner, N. A., Smith, T. M., Stokes, D. C., and Wang, W.: An improved in situ and satellite SST analysis for climate, Journal of climate, 15, 1609–1625, 2002.

640 Roeckner, E., Bäuml, G., Bonaventura, L., Brokopf, R., Esch, M., Giorgetta, M., Hagemann, S., Kirchner, I., Kornblueh, L., Manzini, E., et al.: The atmospheric general circulation model ECHAM 5. PART I: Model description, Accessed March 2020., 2003.

Screen, J. A. and Simmonds, I.: Exploring links between Arctic amplification and mid-latitude weather, Geophysical Research Letters, 40, 959–964, 2013.

Sgubin, G., Swingedouw, D., Drijfhout, S., Mary, Y., and Bennabi, A.: Abrupt cooling over the North Atlantic in modern climate models,
645 Nature Communications, 8, 14 375, 2017.

Stewart, K. D. and Haine, T. W.: Thermobaricity in the transition zones between alpha and beta oceans, Journal of Physical Oceanography, 46, 1805–1821, 2016.

Stommel, H.: The westward intensification of wind-driven ocean currents, Eos, Transactions American Geophysical Union, 29, 202–206, 1948.

650 Tang, Q., Zhang, X., and Francis, J. A.: Extreme summer weather in northern mid-latitudes linked to a vanishing cryosphere, Nature Climate Change, 4, 45–50, 2014.

Tesdal, J.-E., Abernathey, R. P., Goes, J. I., Gordon, A. L., and Haine, T. W.: Salinity trends within the upper layers of the subpolar North Atlantic, Journal of Climate, 31, 2675–2698, 2018.

Vallis, G. K.: Atmospheric and oceanic fluid dynamics, Cambridge University Press, 2017.

655 Woollings, T., Hannachi, A., and Hoskins, B.: Variability of the North Atlantic eddy-driven jet stream, Quarterly Journal of the Royal Meteorological Society, 136, 856–868, 2010.

Wu, Y., Park, T., Park, W., and Latif, M.: North Atlantic climate model bias influence on multiyear predictability, Earth and Planetary Science Letters, 481, 171–176, 2018.

Xie, J., Raj, R. P., Bertino, L., Samuelsen, A., and Wakamatsu, T.: Evaluation of Arctic Ocean surface salinities from the Soil Moisture and
660 Ocean Salinity (SMOS) mission against a regional reanalysis and in situ data, Ocean Science, 15, 1191–1206, 2019.

Yashayaev, I. and Loder, J. W.: Further intensification of deep convection in the Labrador Sea in 2016, Geophysical Research Letters, 44, 1429–1438, 2017.

Zhao, J. and Johns, W.: Wind-forced interannual variability of the Atlantic Meridional Overturning Circulation at 26.5 N, Journal of Geophysical Research: Oceans, 119, 2403–2419, 2014.